Spectropolarimetry of high-redshift obscured and red quasars

Rachael M. Alexandroff, Nadia L. Zakamska, Aaron J. Barth, Fred Hamann, Michael A. Strauss, Julian Krolik, Jenny E. Greene, Isabelle Pâris, Nicholas P. Ross

Monthly Notices of the ROYAL ASTRONOMICAL SOCIETY

MNRAS **479**, 4936–4957 (2018) doi:10.1093/mnras/sty1685
Advance Access publication 2018 June 28

Spectropolarimetry of high-redshift obscured and red quasars

Rachael M. Alexandroff,[1★] Nadia L. Zakamska,[1,2] Aaron J. Barth,[3] Fred Hamann,[4] Michael A. Strauss,[5] Julian Krolik,[1] Jenny E. Greene,[5] Isabelle Pâris[6] and Nicholas P. Ross[7]

[1]*Center for Astrophysical Sciences, Department of Physics and Astronomy, Johns Hopkins University, Baltimore, MD 21218, USA*
[2]*Deborah Lunder and Alan Ezekowitz Founders' Circle Member, Institute for Advanced Study, Einstein Dr., Princeton, NJ 08540, USA*
[3]*Department of Physics and Astronomy, University of California, Irvine, 4129 Frederick Reines Hall, Irvine, CA 92697, USA*
[4]*Department of Physics and Astronomy, University of California, Riverside, CA 92507, USA*
[5]*Department of Astrophysical Sciences, Princeton University, Princeton, NJ 08544, USA*
[6]*Aix Marseille Université, CNRS, LAM, Laboratoire d'Astrophysique de Marseille, F-13013 Marseille, France*
[7]*Institute for Astronomy, University of Edinburgh, Royal Observatory, Blackford Hill, Edinburgh EH9 3HJ, UK*

Accepted 2018 June 23. Received 2018 June 23; in original form 2017 June 29

ABSTRACT

Spectropolarimetry is a powerful technique that has provided critical support for the geometric unification model of local active galactic nuclei. In this paper, we present optical [rest-frame ultraviolet (UV)] Keck spectropolarimetry of five luminous obscured (type 2) and extremely red quasars (ERQs) at $z \simeq 2.5$. Three objects reach polarization fractions of $\gtrsim 10$ per cent in the continuum. We prefer dust scattering as the dominant scattering and polarization mechanism in our targets, though electron scattering cannot be completely excluded. Emission lines are polarized at a lower level than the continuum. This suggests that the emission-line region exists on similar spatial scales as the scattering region. In three objects, we detect an intriguing 90°swing in the polarization position angle as a function of line-of-sight velocity in the emission lines of Ly α, C IV, and N V. We interpret this phenomenon in the framework of a geometric model with an equatorial scattering region in which the scattering material is outflowing at several thousand km s^{-1}. Our model explains several salient features of observations by scattering on scales of a few tens of pc. Our observations provide a tantalizing view of the inner region geometry and kinematics of high-redshift obscured and ERQs. Our data and modelling lend strong support for toroidal obscuration and powerful outflows on the scales of the UV emission line region, in addition to the larger scale outflows inferred previously from the optical emission line kinematics.

Key words: polarization – scattering – quasars: emission lines – quasars: general.

1 INTRODUCTION

The classical unification model of active galactic nuclei (AGNs; Antonucci 1993; Urry & Padovani 1995) explains the difference between unobscured or 'type 1' AGN and obscured or 'type 2' AGN as the result of differences in viewing angle. In this model, a geometrically and optically thick torus of gas and dust surrounds the AGN accretion disc and broad-line region (BLR). Therefore, if the viewer's line of sight points through the torus, most of quasar emission from the accretion disc and the BLR in the optical, ultraviolet (UV) and soft X-rays is obscured. Such an obscured AGN is classified as a 'type 2' object and is characterized at optical and UV wavelengths by little to no continuum emission and an absence of broad lines (e.g. Khachikian & Weedman 1974; Kauffmann et al. 2003; Hao et al. 2005). Quasars are high-luminosity AGNs (typical bolometric luminosities $\gtrsim 10^{45}$ erg s^{-1}), and it is only in the last 15 yr or so that appreciable numbers of type 2 quasars have been identified and the unification model has been extended to high AGN luminosities (Norman et al. 2002; Stern et al. 2002; Zakamska et al. 2003; Stern et al. 2005; Reyes et al. 2008; Treister et al. 2009; Donley et al. 2012; Alexandroff et al. 2013; Yuan, Strauss & Zakamska 2016).

In the local Universe, a convincing case for the geometric unification model was first made using optical spectropolarimetry of nearby type 2 AGN (Antonucci & Miller 1985; Miller, Goodrich & Mathews 1991). Though a direct line of sight to the optical AGN emission is blocked in the geometry of type 2 AGN, this emission can still escape along the unobscured direction perpendicular to the torus and scatter off of free electrons or dust particles in the quasar

★ E-mail: rachael.alexandroff@dunlap.utoronto.ca

host galaxy and into the observer's line of sight. This scattering causes the emission to become linearly polarized, making optical polarimetry and spectropolarimetry the best way to view this scattered emission from the nucleus (Miller & Goodrich 1990; Tran, Cohen & Goodrich 1995).

This process is also presumably occurring in unobscured or type 1 AGN, but linearly polarized optical emission represents a much smaller fraction of the total light in these objects, and the geometry is less favourable (e.g. Borguet et al. 2008). In fact, typical levels of polarization in unobscured AGN are only 0.5 per cent (Berriman et al. 1990). In contrast, optical polarization levels in type 2 quasars at low redshift can reach values of at least a few per cent (Smith et al. 2002, 2003; Zakamska et al. 2005) and occasionally as high as $\gtrsim$20 per cent (Hines et al. 1995; Smith et al. 2000; Zakamska et al. 2005). In addition, light from the BLR scatters into our line of sight by the same process, so the spectrum of a type 2 AGN in polarized light possesses broad emission lines (e.g. Antonucci & Miller 1985; Zakamska et al. 2005). Thus, high measured levels of polarization and broad emission lines seen only in polarization are a tell-tale sign of obscured active nuclei in the classical orientation model. Indeed, it was imaging polarimetry and later deep spectropolarimetry that confirmed the presence of hidden AGN at the centers of radio galaxies – demonstrating that these objects were, in fact, radio loud type 2 AGN (see Antonucci 1993; Vernet et al. 2001; Tadhunter 2005, and references therein).

Few, if any, spectropolarimetric observations of radio-quiet obscured quasars at the peak of galaxy formation ($z \sim 2.5$) are available because, until recently, such objects could not be readily identified. Furthermore, obscured quasars are by definition very faint at rest-frame optical and UV wavelengths, whereas spectropolarimetry requires high signal-to-noise (S/N) ratio observations to detect polarized flux at the level of a few per cent. Therefore, we can only perform polarimetry and especially spectropolarimetry of high-redshift obscured quasars with large telescopes and/or long integration times. Alexandroff et al. (2013) reported the results of spectropolarimetry performed on two high-redshift ($z \sim 2.5$) rest-frame UV-selected type 2 quasar candidates using the CCD spectropolarimeter (Schmidt, Stockman & Smith 1992) at the 6.5-m MMT telescope. They demonstrated the presence of a polarization signature at the level of a few per cent, but low (S/N) ratios and availability of data for only two objects made further interpretation difficult.

While it is clear what polarization signal is expected from a quasar obscured by a classical torus (type 2), perhaps not all quasars possess a classical obscuring region. For example, Sanders et al. (1988) and Hopkins et al. (2006) argue that some obscured quasars may represent a particular phase in quasar evolution after a merger or an instability within the galactic disc enshrouds the object in gas and dust. If this is the case, obscuration may originate on galaxy-wide scales. We then might expect a population of objects where the openings in the obscured material are not well-organized in a conical structure. Red quasars at both low (e.g. Smith et al. 2000; Glikman et al. 2007; Urrutia et al. 2009; Glikman et al. 2012, 2013) and high (Eisenhardt et al. 2012; Wu et al. 2012; Tsai et al. 2015; Banerji et al. 2015; Ross et al. 2015; Hamann et al. 2017) redshift may be undergoing a phase of quasar evolution where the obscuring region is not a classical torus as evidenced by the presence of galaxy-wide outflows (Zakamska et al. 2016) and merger signatures (Glikman et al. 2015). Such objects would not have symmetric scattering regions (an example source was presented by Schmidt et al. 2007), and thus would have a lower net polarization fraction than classical type 2 quasars.

In this work, we use spectropolarimetry to probe the geometry of obscuration of high-redshift type 2 quasars and extremely red quasars (ERQs). We present observations of five such objects conducted with the low resolution imaging spectrometer (LRIS; Oke et al. 1995) in polarimetry mode (Goodrich, Cohen & Putney 1995). We describe our sample selection as well as observations and data reduction in Section 2. Then, Section 3 describes our data analysis and results followed by a discussion of those results in Section 4. We introduce our proposed model in Section 4.1 and summarize our conclusions in Section 5.

Throughout this paper, we adopt a cosmology with $h = 0.7$, $\Omega_m = 0.3$, and $\Omega_\Lambda = 0.7$. We use SDSS Jhhmm+ddmm notation throughout the text (full coordinates are listed in Table 1) with an additional marker letter to represent how the source was originally identified (see Section 2.1 for more details). Throughout, U and Q refer to Stokes flux densities while u and q refer to Stokes parameters relative to the total continuum.

2 SAMPLE SELECTION, OBSERVATIONS, AND DATA REDUCTION

2.1 Parent sample

Our sample consists of five obscured quasars selected using two distinct methods: two type 2 quasar candidates at redshift $z \sim 2.5$ (Alexandroff et al. 2013), two ERQs at the same redshift (Ross et al. 2015; Hamann et al. 2017), and one object taht meets the criteria of both selection methods (Table 1). We briefly describe the parent sample selection methods below. We were particularly interested in searching for evidence of differences in the covering factor of obscuration (as traced by the polarization fraction) between these two populations.

Two of our sources, which we mark with a 'T' at the end of the designation, SDSSJ1515+1757T and SDSSJ1623+3122TE, were originally selected from the Sloan Digital Sky Survey (SDSS) Baryon Oscillation Spectroscopic Survey (BOSS; Dawson et al. 2013) by their narrow line widths (full width at half-maximum (FWHM) <2000 km s^{-1} in both C IV and Ly α) and weak continuum in the rest-frame UV, to form an optically selected sample of high redshift type 2 quasar candidates (for more details see Alexandroff et al. 2013). Only objects from Data Release 9 (Ahn et al. 2012) or earlier were included in this search, which yielded a sample of 145 type 2 quasar candidates.

An additional three sources, labelled with an 'E', SDSSJ1232+0912E, SDSS1652+1728E and SDSSJ2215 − 0056E, were selected based upon a combination of data from the SDSS and the *Wide-Field Infrared Survey Explorer* (*WISE*; Wright et al. 2010) AllWISE data release[1] (Ross et al. 2015; Hamann et al. 2017). This selection targeted objects with high infrared-to-optical ratios expected in obscured quasars. A sub-sample of these red objects shows unusual spectroscopic properties including large rest equivalent width (REW) emission lines ($\gtrsim$100 Å), unusually high N V/Ly α ratios and emission lines with high kurtosis (lacking the typical broad wings of gaussian emission lines). These objects were labelled ERQs. A final sample of 97 ERQs in the redshift range of $2.0 < z < 3.4$ was selected to have a colour between the SDSS i band and the *WISE* $W3$ band (12 μm) ≥ 4.6 mag and a measured REW of C IV >100 Å, producing the Hamann et al. (2017) sample.

[1] http://irsa.ipac.caltech.edu/

Table 1. Type 2 quasars and ERQs with spectropolarimetric observations.

Short Name	RA	Dec.	z	r	C IV	C IV	[O III]	log	$i-W3$	type
			$L_{[\mathrm{O\,III}]}$	mag	FWHM	kt_{80}	FWHM			
	hh:mm:ss	dd:mm:ss		AB	km s^{-1}		km s^{-1}	erg s^{-1}	AB	
SDSSJ1232+0912E	12:32:41.73	+09:12:09.37	2.374	21.11 ± 0.05	4787 ± 52	0.37	5627	43.92	6.8	ERQ
SDSSJ1515+1757T	15:15:44.00	+17:57:53.06	2.402	22.24 ± 0.12	1118	–	856.4	43.98	2.0	T2
SDSSJ1623+3122TE	16:23:27.66	+31:22:04.29	2.344	21.60 ± 0.09	1572 ± 68	0.34	658.3	44.08	4.5	T2E
SDSSJ1652+1728E	16:52:02.64	+17:28:52.38	2.942	20.38 ± 0.02	2403 ± 45	0.33	1461	44.87	5.4	ERQ
SDSSJ2215 − 0056E	22:15:24.00	−00:56:43.80	2.493	22.27 ± 0.12	4280 ± 112	0.37	3057	43.64	6.2	ERQ

Note: Type 2 quasars and ERQs presented in this paper. Our targets span a range of properties in their line widths and colours. Position and redshift information are from the SDSS Sky server Data Release 12. C IV FWHM, REW, and kt_{80} were measured by Hamann et al. (2017) for four objects. Measurements for SDSS1515+1757T are taken from the SDSS Sky server Data Release 12. For SDSSJ1232+0912E and SDSSJ2215 − 0056E, [O III] FWHM and luminosity are from Zakamska et al. (2016), and for the remaining objects these measurements are from the Gemini-North data presented in Section 2.2.

There is also some overlap between the two samples. While SDSSJ1652+1728E does not meet the strict cutoff required of the Alexandroff et al. (2013) sample of type 2 candidates, we note its relatively narrow FWHM in C IV (<2500 km s^{-1}). Additionally, SDSSJ1623+3122TE was primarily selected as a type 2 quasar candidate, but is also listed as part of the 'expanded' sample of ERQs, defined to have 'ERQ-like' line properties even if they are less red than the principal sample in $i - W3$ colours (Hamann et al. 2017). We label it TE in Table 1 to denote this joint classification. Both the Alexandroff et al. (2013) and the Hamann et al. (2017) methods aim to select obscured quasars at high redshifts. While we still do not fully understand the physical properties of each of these populations, SDSSJ1623+3122TE and SDSSJ1652+1728E demonstrate that there can be some overlap between the methods.

2.2 Rest-frame optical properties

SDSS covers the rest-frame UV at the redshift of our objects, and therefore follow-up near-infrared (NIR) spectroscopy is necessary to probe their rest-frame optical properties. For the purposes of the current study, we use the NIR (rest-frame optical) spectra primarily to distinguish between classical type 1 and type 2 objects and to look for outflow signatures.

The [O III] λ5007 Å+H β spectra for all five targets studied in this Keck program are shown in Fig. 1, with three objects at the top from our new program on the Gemini Near-Infrared Spectrograph (GNIRS) on board Gemini-North and two objects at the bottom from the previously published XSHOOTER program (Zakamska et al. 2016). Our new GNIRS data were obtained in semester 15 A in queue mode (PI: Alexandroff). The instrument was operated in cross-dispersed mode using the 1/32-mm grating and with a slit width of 0.45 arcsec to provide full wavelength coverage from 0.9 to 2.5 μm, which covers H α, H β, and [O III] in the rest frame of our objects. Each object was observed in queue mode for a total of 60 min in a series of nodded 300-s exposures along the slit. Data reduction was performed using the XDGNIRS package v2.0 (Mason et al. 2015), a wrapper script for the PYRAF tasks in the Gemini IRAF package. The script was run in interactive mode and the data were examined at each step in the process. As our targets are faint point sources, we manually set the position of the aperture for the trace of each order rather than having the program find it automatically.

Using the calibrated one-dimensioanl (1D) spectra, we performed multi-Gaussian emission-line fits as described by Zakamska et al. (2016). Briefly, [O III] λ4959 Å and [O III] λ5007 Å are assumed to have the same velocity structure and a fixed-flux density amplitude ratio of 0.337. Beyond this assumption, our fits are either 'kinematically tied' – i.e. the same velocity structure is assumed for [O III] and H β – or 'kinematically untied', in which H β has velocity structure that is different from [O III]. Our null hypothesis is that in type 2 quasars, [O III] and H β are kinematically tied and their typical ratio is 10:1, with the caveat that both of these characteristics can be affected by strong outflows (Zakamska & Greene 2014; Zakamska et al. 2016).

Unlike low-redshift type 2 quasars selected to have narrow Balmer lines, follow-up observations in the rest-frame optical (Greene et al. 2014) of 25 objects from our parent sample of type 2 quasar candidates showed that ∼90 per cent of objects displayed a broad H α or H β line and all had intermediate values of extinction ($0 < A_V < 2.2$ mag) akin to type 1.8/1.9 quasars. Yet, both SDSSJ1515+1757T and SDSSJ1623+3122TE – selected based on their narrow high-equivalent-width UV lines (Alexandroff et al. 2013) – show classical type 2 quasar features in the rest-frame optical: They have weak continua, narrow H β that has the same velocity structure as [O III], and [O III]/H β ratios of 9.9 and 6.9, respectively. These specific objects were chosen for spectropolarimetry follow-up because they are unambiguously high-redshift type 2 quasars. SDSSJ1515+1757T shows no sign of [O III] outflows, whereas SDSSJ1623+3122T has a noticeable blue-shifted component in its [O III] emission.

SDSSJ1652+1728E has a mix of features. While it is best fitted with a kinematically tied model with [O III]/H β = 7.7, the rest-frame optical continuum is relatively strong and marginally inconsistent with a type 2 classification. In addition, the REW of [O III] λ5007 Å of 213 Å is intermediate between type 1s and type 2s at these luminosities (Greene et al. 2014). This object shows a strongly kinematically disturbed [O III], with the width containing 80 per cent of the line power of w_{80} = 1760 km s^{-1}, which is in the upper ∼5 per cent of [O III] velocity width in the $z < 1$ type 2 population (Zakamska & Greene 2014).

The remaining two targets, SDSSJ1232+0912E and SDSSJ2215 − 0056E, are ERQs. In the rest-frame optical, they have a mix of type 2 and type 1 characteristics as described in detail in Zakamska et al. (2016). The rest-frame optical spectra for SDSSJ1232+0912E is fitted with a kinematically untied model while in the case of SDSSJ2215 − 0056E there is no preference between the kinematically tied and untied ones. The REW of [O III] λ5007 Å for both is intermediate between expected type 1 and type 2 values. Both objects have extremely fast [O III] outflows– the FWHMs measure as 5630 and 3060 km s^{-1}, respectively. Because [O III] has a relatively low critical density, it must originate on relatively large scales, ≫100 pc (Hamann et al. 2011; Zakamska et al. 2016). The [O III] velocities seen in ERQs are too large to be contained by any reasonable galaxy potential and perhaps indicate

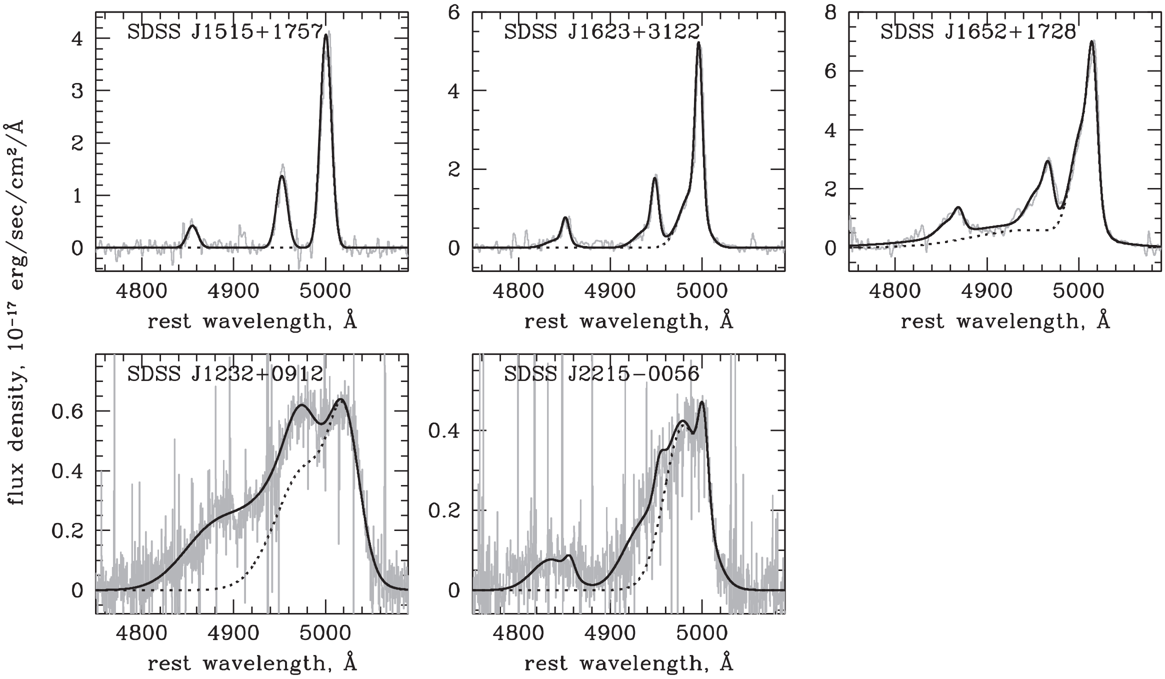

Figure 1. The continuum-subtracted [O III]+H β complex and best fits for the five objects studied in this paper. The spectra were obtained for the top three objects with GNIRS and have not previously been published. Spectra for the bottom two objects were obtained with the VLT XSHOOTER and were published in Zakamska et al. (2016). The grey histograms show the data, the solid black line shows the best overall fit, and the dotted black line shows the [O III] λ5007 Å fitted profile separately. In SDSSJ1515+1757T, SDSSJ1623+3122TE, and SDSSJ1652+1728E, the best fits are kinematically tied (i.e. [O III] and H β have the same velocity structure), and the best velocity fit is comprised of one, two, and three Gaussian components, respectively. The best fits for SDSSJ1232+0913E and SDSSJ2215 − 0056E were previously presented in Zakamska et al. (2016) and are reproduced here. In SDSSJ1232+0913E, the best fit is kinematically untied; in SDSSJ2215 − 0056E, it is kinematically tied; in both cases, two Gaussian components are used for [O III].

that these quasars are in the predicted 'blowout' phase of quasar activity (Hopkins et al. 2006).

The five objects presented here were selected for follow-up with Keck LRISp to be either type 2 quasars with classifications confirmed with NIR spectroscopy or to be ERQs with strong signs of galaxy-scale outflows. Thus, this sample allows us to probe the obscuring geometry and scattering efficiency of obscured quasars selected by two different methods.

2.3 Observations and data reduction

Data for this project were obtained as part of a NASA time allocation on the Keck Telescope in semester 2015A. All observations were conducted over the course of a single night (UT 2015-05-22) on Keck I from Keck Headquarters in Waimea in clear conditions with seeing around 0.6 arcsec. The observational setup was chosen to maximize S/N ratio over resolution for our faint targets and to put the relevant emission lines of Ly α and C IV on the blue side CCD, where cosmic ray (CR) effects are less strong than on the red side. We used a 1.0-arcsec slit width and the D68 dichroic to separate the light into blue and red beams. The blue side spectrograph used a 300 grooves mm^{-1} grism, giving a dispersion of 1.43 Å pixel^{-1}, whereas the red side used a 400 grooves mm^{-1} grating, which gave a dispersion of 1.16 Å pixel^{-1}. This blue side grism provides some level of contamination on the red end due to second-order light at $\lambda \gtrsim 6400$ Å. No binning either spatially or spectrally was applied during observations. The combined wavelength coverage from both the blue and red sides stretched from 3100 to 10 300 Å, with a small overlap at ∼6500–6800 Å. Calibration darks, dome flats, and arcs were taken the afternoon before the start of observations, with additional dome flats taken at the end of the evening.

All science targets were observed in a standard sequence of exposures with four positions of the rotatable half-wave plate (0°, 45°, 22°.5, and 67°.5) lasting 600 s on the blue side and 520 s on the red side to synchronize the ends of the exposures due to the differing read-out times. Four quasars were observed for two full observation sequences for a total observed time of 4800.0/4160.0 s on the blue and red sides, respectively. SDSSJ2215 − 0056E was observed for a single full sequence – half the exposure of the other objects – due to timing constraints. In addition, we observed the flux standard star Feige 34, the null (unpolarized) standard stars HD 109055 and BD+28°4211 (also a flux standard), and the polarized standards HD 155528 and HD 204827. All observations were done at the parallactic angle except for the special case of SDSS1652+1728E described further below.

CR hits were removed from the raw blue side science images using the IRAF imaging version of L.A. cosmic (van Dokkum 2001). In the red detectors, 300-μm thick Lawrence Berkely Nationla Laboratory CCDs (Rockosi et al. 2010), a single CR hit appears as a trail spanning more individual pixels than on the blue side CCDs. Because each Stokes parameter is measured using four separate beam spectra and differencing pairs of spectra, any error in cleaning CRs is multiplied four-fold for a single Stokes parameter and eight-fold for the polarization fraction or polarization position angle due to the total number of pixels affected per measurement. Thus, the red side CCDs suffer so acutely from CR contamination that the data were unusable.

Data reduction and calibration were conducted following the methods of Miller, Robinson & Goodrich (1988) and Barth, Filippenko & Moran (1999). In brief, bias subtraction, flat fielding, spectral extraction, wavelength, and flux calibration were first performed using IRAF, and polarization measurements were performed using routines written in IDL. Uncertainties due to photon-counting statistics and detector readout noise were propagated at every step of the reduction process, yielding error spectra for the Stokes parameters Q and U. Extraction regions were 24 pixels wide (corresponding to 3.24 arcsec) except for SDSS1652+1728E, which had a different spatial profile described below. The background region was calculated over 10 pixels (corresponding to 1.35 arcsec) above and below the extraction region and an additional 10 pixels away from the extraction region. A wide extraction region was used because the science targets were very faint.

SDSS1652+1728E is point-like in the SDSS images. There is another point-like source 1.6 arcsec away, which does not have SDSS spectroscopy. During the observations, we placed the slit to cover both objects and to determine whether the second object might be physically related. The spectra of this companion showed no features and upon further inspection, its SDSS photometric colours ($u - g = 0.97$, $g - i = 0.58$) place it in the stellar locus for SDSS point-like objects (Yèche et al. 2010). The presence of this likely foreground star in the slit makes proper extraction of SDSS1652+1728E complicated as the sources are so close as to be blended in the 2D spectra. We moved the background region an additional 10 pixels away and made the extraction region only 20 pixels to avoid the additional source.

The extracted spectra were rebinned to 2 Å bin^{-1} prior to polarimetry analysis. Then, very fine wavelength alignment (to within 0.1 Å) was done using the cross-correlation of all eight available extracted spectra for a single object. The zero point of the polarization angle was calibrated by normalizing to the published value for HD15528 (Clemens & Tapia 1990) of 105°.13. We find that calculated polarization values and angles for our polarized standards agreed well with published values. For HD15528, we measure a polarization of 4.979 per cent in the V-band (mean $\lambda \sim 5388$ Å and $\Delta\lambda \sim 352$ Å) compared to 4.849 for the originally published value (Clemens & Tapia 1990). For HD204827, we measure a polarization of 5.760 per cent with a polarization position angle of $\theta = 59.°48$ in the B-band (4000–5000 Å). This is extremely close to the published values of $P = 5.648 \pm 0.022$ per cent and $\theta = 58.°20 \pm 0.°11$ in Schmidt, Elston & Lupie (1992). In addition, observations of unpolarized standard stars show well-behaved, flat response over the entire observed wavelength range and give a calculated polarization of 0.08 per cent. Though this measurement includes some combination of the stellar and instrumental polarization, it gives us an approximate upper limit on the effects of instrumental polarization.

We conducted a variety of consistency checks with our data to convince us of the accuracy of our results. We measured the polarization for each sequence of exposures separately to make sure they were consistent before we combined them using a simple algorithm which weights each half equally. We also checked that the normal and optimal weighting algorithms (Horne 1986) for the source extraction give similar results. We used the optimal weighting algorithm except when we measured the line polarization for SDSS1515+1757T and SDSS1623+3122TE, where the results did not agree well. It is also encouraging that clear detections of polarization in the continuum showed consistent values of the observed polarization angle in adjacent wavelength bins except in cases where the polarization angle can clearly be seen to physically vary as a function of wavelength (see Section 3 for more information).

All polarization measurements were then made in the q and u spectra and converted to a debiased polarization and position angle, following the steps outlined in Miller et al. (1988). To increase S/N in the continuum, we binned over several hundred angstroms for each measurement. We were careful not to include wavelengths on the very red edge of the blue CCD to avoid the second-order light due to the blue side grism. Polarization fractions and angles as well as the wavelength range over which each was calculated are listed in Table 2. The usual definition of polarization is a positive-definite value, $p = \sqrt{q^2 + u^2}$, which becomes problematic in our regime of low S/N. Instead, we report the debiased polarization that has a better behaved error distribution, $p = \pm\sqrt{\left|q^2 + u^2 - \sigma_q^2 - \sigma_q^2\right|}$, where the overall sign is set by the value within the absolute value signs. Thus, if a measurement is dominated by measurement error, the quantity $q^2 + u^2 - \sigma_q^2 - \sigma_u^2$ will have a value less than zero, and the debiased polarization will be negative. In cases where the debiased polarization is dominated by measurement error, we instead report 2σ upper limits. The total flux spectra as well as continuum polarization, q and u normalized Stokes parameters and position angle measurements are shown in Fig. 2 as well as the Appendix.

All our targets lie at relatively high Galactic latitudes with a range of $34.°0 < |b| < 71.°5$, and thus the contribution to the polarization from interstellar dust is expected to be quite low. In fact, Serkowski, Mathewson & Ford (1975) demonstrated that the Galactic interstellar polarization is $\lesssim$9 per cent $\times$ $E(B - V)$. We check the measured values of $E(B - V)$ along the sightlines to our targets from both Schlegel, Finkbeiner & Davis (1998) and Schlafly & Finkbeiner (2011) and find values in the range $0.0206 < E(B - V) < 0.1179$ mag, implying interstellar polarizations of $\lesssim$1 per cent, much smaller than any of the values we are measuring in our targets. Thus, we conclude that interstellar polarization has a negligible effect on our measured polarization values.

3 RESULTS

Our sample spans a range of rest-frame optical properties as described in Section 2.2, from classical type 2 spectra with quiescent [O III] kinematics to extreme [O III] outflow activity. Here, we discuss the results of our spectropolarimetry analysis and connect them to other known multiwavelength properties of our targets.

In Fig. 2 and Appendix A, we present the Keck LRISp data for each of our objects. One object, SDSS16521+1728E (Fig. 2), has considerably higher S/N than the other objects, and thus we often use it as an example of several trends. We display the high sensitivity total UV spectrum in the first panel. The following panels show binned quantities for the normalized Stokes parameters q and u, the polarization fraction, and polarization position angle in bins designated by the horizontal axis error bars (and listed in Table 2). We also display the full polarization position angle as a function of wavelength in the emission lines (smoothed using a least-squares polynomial smoothing filter with a window of seven pixels) to display variations within the lines as a function of velocity. In the following sections, we discuss the trends we see in our spectra.

3.1 Level of continuum polarization

In Table 2, Fig. 2, and the Appendix, we present continuum polarization measurements in several continuum regions, chosen in the rest-frame of the quasar to avoid contamination by UV emission lines. The level of continuum polarization just blueward of C IV (rest frame 1425–1525 Å) spans from 15.7 ± 0.4 per cent in SDSSJ1652+1728E to consistent with zero in SDSSJ2215 − 0056E.

Table 2. Continuum and line polarization fractions.

Short Name	1250–1350 Å	1425–1525 Å	1550–1650 Å	1650–1750 Å	1750–1850 Å	Ly α	N V	C IV
SDSSJ1232+0912E	7.7 ± 1.9	12.1 ± 4.0	12.4 ± 2.0	17.4 ± 2.7	17.0 ± 1.5	7.5 ± 0.8	3.4 ± 0.4	5.8 ± 0.4
SDSSJ1515+1757T	<6.5	11.0 ± 3.2	<1.8	9.4 ± 2.6	10.2 ± 3.5	8.8 ± 0.9	5.3 ± 3.5	7.0 ± 1.3
SDSSJ1623+3122TE	<5.2	6.5 ± 3.8	8.5 ± 1.7	7.0 ± 3.0	2.1 ± 2.3	9.6 ± 1.0	5.3 ± 3.0	5.6 ± 1.1
SDSSJ1652+1728E	16.2 ± 0.3	15.7 ± 0.4	13.8 ± 0.3			3.2 ± 0.2	4.0 ± 0.1	4.9 ± 0.2
SDSSJ2215 − 0056E	<14.7	<4.9	<1.3	<6.9	<9.1	1.8 ± 1.3	1.5 ± 2.0	<1.2

Note: Polarization fractions of our targets as a function of rest wavelength. All measurements are listed as percentage of the total flux. For emission lines, the polarization was measured over the wavelength range corresponding to the FWHM of C IV for each object. Upper limits are 2σ.

In our sample of five sources, four (both type 2 quasars and two of the ERQs) are consistent with polarization fractions significantly greater than 3 per cent – a high polarization fraction for non-synchrotron sources. Three of the five have polarization fractions >10 per cent. Overall, the polarization values measured are much higher than those observed in type 1 AGN. For example, Berriman et al. (1990) found an average polarization of 0.5 per cent for the 114 quasars from the Palomar-Green Bright Quasar Survey with a maximum polarization of 2.5 per cent. This is expected as type 1 AGNs are dominated by direct quasar light that would dilute any polarization signal. In Alexandroff et al. (2013), we measured the polarization of two type 2 quasar candidates but unlike our current sample designated with a 'T', these objects were not pre-selected to be unambiguous type 2 quasars based on their rest-frame optical spectra. We found of polarization >5 per cent in the blue continuum of one object, SDSSJ220126.11+001231.5, and an average polarization further redward of 1.9 ± 0.3 per cent, higher than could be accounted for by a typical unobscured quasar combined with instrumental systematics ($\lesssim$0.1 per cent) and Galactic polarization (<0.8 per cent). The second object observed in that paper, SDSSJ004728.77+004020.3, had an average continuum polarization of only 0.91 ± 0.35 per cent, making our interpretation of the nature of the source less clear. Contamination from unpolarized quasar continuum is possible in these objects.

Perhaps, the best context for our sample is a direct comparison to other verified type 2 AGN, radio galaxies, or other samples of red quasars. Zakamska et al. (2005) measure a polarization >3 per cent in 9 of 12 luminous type 2 quasars at $z \sim 0.5$ and a mean polarization of 5.7 per cent for all 12 objects, with a maximum polarization of 15.4 per cent at rest wavelengths between 2800 and 6500 Å. They contend that the high polarization is due to dust scattering and that all but one object are essentially uncontaminated by the host galaxy which is the main dilution mechanism of the intrinsic polarization fraction in type 2 AGN.

Two IR-bright, type 1 quasars, IRAS 13349+2438 and IRAS 14026+4341 (also a BAL quasar), have been studied with polarimetry in the rest-frame UV (Hines et al. 2001). They exhibit high-polarization fractions at their bluest wavelengths (9.44 per cent between rest-frame 2000–2700 Å and 14.84 per cent between rest-frame 1690–2270 Å, respectively) while reaching a maximum polarization at around 3000 Å with the host galaxy contributing at most 10 per cent of the light at these wavelengths. Of the entire IR-bright sample observed in optical polarization, 50 per cent show polarization fractions >3 per cent. Similarly, Smith et al. (2000, 2002, 2003) studied the polarization properties of a sample of two Micron All-Sky Survey (2MASS)-selected red AGN with $M_{K_s} < -23$ and $J - K_s > 2$. This sample includes both type 1 and type 2 AGNs with a mean redshift of $z = 0.25$. Smith et al. (2002) showed that in a sample of 70 2MASS quasars with optical broadband polarimetry, 10 per cent were polarized with $p > 3$ per cent with a maximum polarization measured of 11 per cent. At these redshifts, host galaxy light is likely a significant contaminant to the continuum luminosity ($\gtrsim$50 per cent), so the intrinsic polarization fractions are likely higher.

We argued in Alexandroff et al. (2013) that the rest-frame UV continuum in high-redshift type 2 candidates from SDSS was too luminous to be explained by the host galaxy alone and too blue to be explained by the reddening of the intrinsic quasar light. There were two competing hypotheses for the origin of this emission. The first is that the observed UV continuum may be due to a 'patchy' geometry allowing some direct sightlines to the quasar. The second is that the central quasar is completely obscured from view while all of the UV continuum is due to scattered light. Similar ideas were discussed for the origin of the rest-frame UV continuum of ERQs and other red quasars (Assef et al. 2016; Zakamska et al. 2016; Hamann et al. 2017). From the comparison with other available samples, we find that the continuum polarization of our targets is at the high end of the polarization fraction distribution for obscured and red quasars. Detecting such high values of continuum polarization in our targets is unambiguous confirmation that most of the continuum emission is due to anisotropic scattered light.

Another paradigm we are testing with our data is that of the geometry of scattering. Is the circumnuclear obscuration axisymmetric, in which case we expect an elongated scattering region with relatively minor geometric cancellation of polarization and therefore high polarization values? Or is the nucleus largely enshrouded, with several randomly oriented scattering regions (Schmidt et al. 2007), where we can expect geometric cancellation of polarization and therefore low polarization values? With our admittedly small sample, we find no relationship between the rest-frame optical type (type 2, ERQ) or the presence of [O III] outflows and the continuum polarization level that might be expected if a difference in optical type or outflow velocity denoted a difference in quasar evolutionary state or obscuring geometry.

3.2 Wavelength dependence of continuum polarization

Scattering of the continuum can be due to dust or free electrons in the ionized gas. The expected polarization fraction due to electron scattering is described by the Thomson formula and is independent of wavelength. For dust scattering, the polarization fraction may vary as a function of wavelength depending on the dust composition and size distribution (e.g. Zubko & Laor 2000). In this section, we discuss the trends seen in our sample, with more details discussed in Section 4.4.

There is marginal evidence for a wavelength dependence in the polarization fraction in the continuum of our objects, with the polarization fraction appearing to rise at longer wavelengths. Such a trend is particularly evident in SDSSJ1232+0912E. Unfortunately, our achievable sensitivity makes it difficult to determine if this

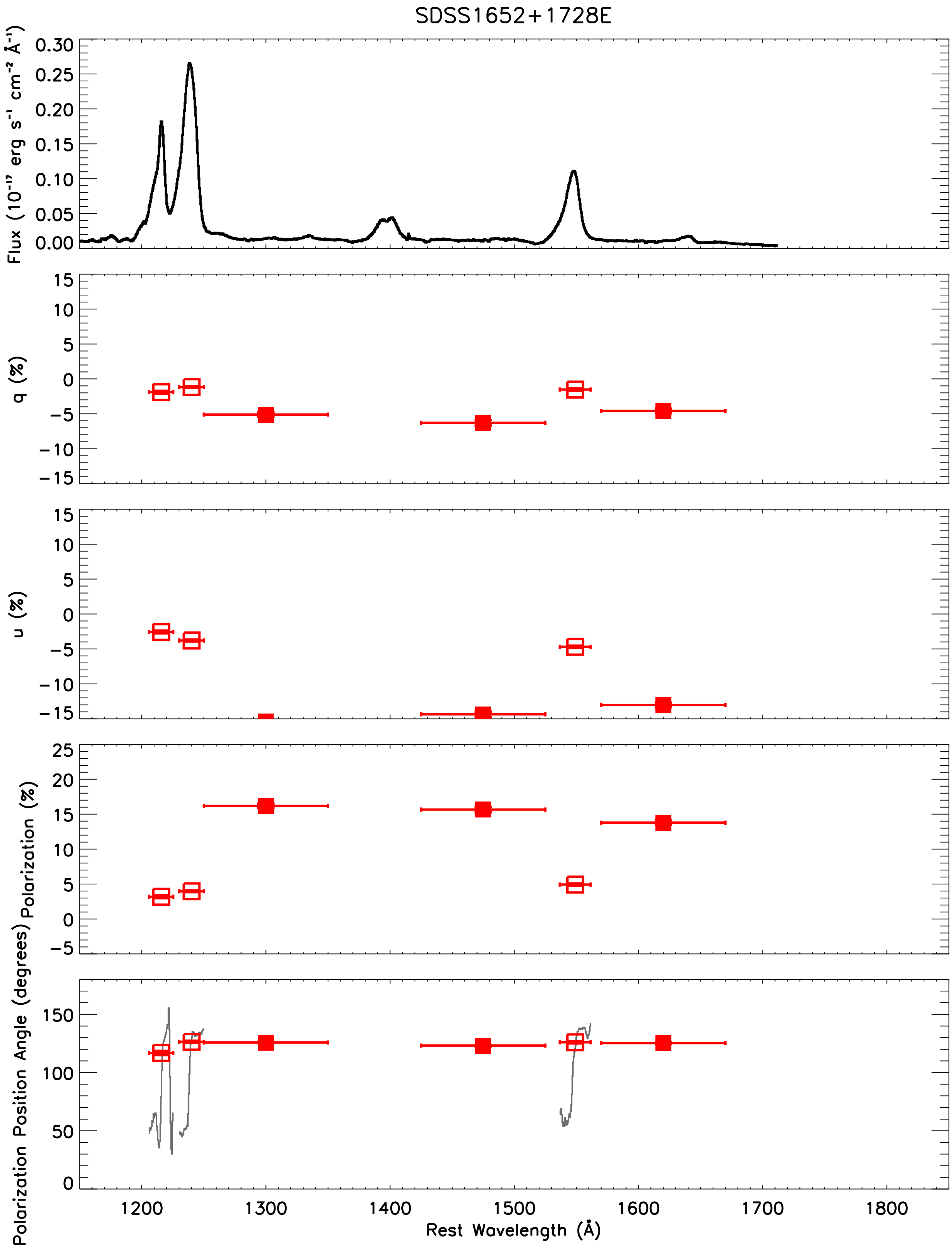

Figure 2. LRISp spectra of our highest S/N target (all others are displayed in a similar manner in Appendix A). The top panel shows the total flux spectrum. The second and third panels show the normalized Stokes parameters *q* and *u* binned over the wavelength range as indicated by the horizontal axis error bars (same as Table 2). The fourth panel shows the continuum polarization and statistical error in that measurement over the same bins, and the bottom panel shows the same for polarization angle. For data points, where the debiased polarization is uncertain, we plot the 2σ upper limit. The filled squares represent continuum measurements while the open squares represent emission line measurements. In grey, we include the smoothed polarization position angle (7-pixel bins) in the emission lines.

trend is real, as most of the variation is within the observed error bars. Alexandroff et al. (2013) found that there was evidence for wavelength-dependent polarization fraction in one object that was strongest at bluer wavelengths, the opposite of what we observe in SDSSJ1232+0912E.

An increasing polarization fraction at redder wavelengths suggests either that the polarization is wavelength-dependent and therefore likely caused by dust or that the continuum is contaminated by blue unpolarized light (such as unpolarized quasar continuum) that dilutes our polarization signal at bluer wavelengths. However, the evidence for this wavelength dependence is marginal at best so we will defer any discussion of wavelength-dependent polarization in our objects for future work.

3.3 Overall polarization of emission lines

The observed level of polarization in emission lines relative to the continuum is a good indicator of the geometry and polarization mechanism of the emission lines. In particular, the polarized fraction of the emission lines relative to the continuum can indicate the scale of the scatterer. If the emitting region and the scattering region are on the same scale, the polarization is diluted by geometric effects as there is no single scattering direction. Higher values of the ratio of emission line to continuum polarization imply scattering on large scales, beyond the line emitting regions, so that the lines remain as polarized as the continuum. Similarly, lower values of this ratio imply that the scattering is on scales closer to or within the emission line region and thus the line emission is only marginally polarized. Geometric dilution in emission line regions relative to the continuum is found in many AGN sources (e.g. Stockman, Hier & Angel 1981; Glenn, Schmidt & Foltz 1994; Goodrich & Miller 1995; Tran 1995) and implies that the scattering region is on a similar, or slightly larger scale, than the emission region.

We consider the UV emission lines of Ly α, N V, and C IV, integrating over the FWHM of C IV (see Table 1). In all cases, the observed polarization fractions of the emission lines are lower than the continuum polarization with the exception of the quasar SDSSJ1623+3122TE. Nevertheless, polarization values can still reach levels of >8 per cent in the Ly α emission line, most notably in SDSSJ1515+1728T and SDSSJ1623+3122TE.

We calculate the ratio of the line polarization fraction (for Ly α, N V, and C IV) to the continuum polarization fraction just blueward of C IV between 1425 and 1525 Å and find some evidence that those objects designated as classical type 2 quasars in our sample show higher values of this ratio. The mean and the sample standard deviation over all six lines for our two ERQs (excluding SDSSJ2215 − 0056E, where there is not a high enough S/N ratio in the lines) is 0.36 ± 0.14, whereas for the two type 2 quasars it is 0.85 ± 0.31. The ratio of the line to continuum polarization measures the geometric mixing of polarization as emission propagates from the emission-line region and scatters off the scattering medium. Thus, our measured ratios imply that the scattering regions for classical type 2s may be on larger scales than the scattering regions in ERQs.

This geometric interpretation becomes more complicated if resonant scattering has a strong effect on the measured emission line polarization fractions, but in Section 4.4 we consider and reject the possibility of resonant scattering as the source of polarization in the emission lines of our objects. As a result, the smaller polarization fractions measured in the emission lines as compared to their continuum polarization fraction – especially in ERQs – implies that the emission-line regions suffer from geometric dilution, and therefore the scatterer is on similar scales to the emission line region.

3.4 Kinematics of line polarization

We observe a significant variation in the polarization fraction across emission lines. The polarization fraction tends to reach a minimum around the line centroid and a maximum at a redshift between +1000 and +2000 km s^{-1}. This pattern is perhaps most pronounced in SDSSJ1652+1728E (Fig. 3). Such wavelength-dependent polarization in emission lines is present in several objects in our sample and may provide a unique window into our understanding of the scattering geometry. We discuss this further in Section 4.

Perhaps, the most intriguing trend we observe is the wavelength dependence of the polarization position angle across all emission lines. This trend can be observed in SDSSJ1515+1728T, SDSSJ1623+3122T, and most dramatically in SDSSJ1652+1728E. This observed trend has several key features. First, the polarization position angle appears to vary by almost exactly $\pi/2$ radians across the emission line (see Figs 3 and A2). Most notably for our analysis, the polarization position angle of the continuum is the same as the polarization position angle of the emission lines at their red wings. This trend can easily be observed in Fig. 3, but is also apparent as a change in the ratio of the q and u normalized Stokes parameters in Fig. 4. This format is inspired by similar figures for the study of polarization in supernovae (SNe; for a review see Wang & Wheeler 2008).

If there were a single, smooth, and axisymmetric scattering region where the polarization was independent of wavelength, we would find a consistent polarization fraction that would result in a clustering of all data points in the q/u plane. If, instead, there is some form of homologous expansion of the scattering material ($v \propto r$), then at each wavelength the viewer would see a different slice or shell in the expanding scattering material. Each slice has a different optical depth that would introduce a wavelength dependence to the polarization and thus cause the data points to spread out in a line in the q/u plane, also known as the 'dominant axis' (Hoeflich et al. 1996; Wang et al. 2001). This may be what is observed in the N V emission line in SDSSJ1652+1728 (see Fig. 4), implying that the emission line gas in our sources may show varying degrees of smoothness.

Deviations from this straight line in the q/u plane then represent deviations from the assumptions of smoothness or axisymmetry in the scattering geometry as seen in the Ly α and C IV emission lines of SSSJ1652+1728 most prominently. These deviations must be finite to maintain the presence of a single dominant axis in the plane (e.g. the presence of clumpy material). This model ignores scattering in the interstellar medium of our galaxy, which can cause a rotation in the polarization position angle though usually of only a few degrees. It also does not include scattering of continuum photons in resonance with emission lines that can change the polarization position angle if the geometry of the continuum scattering region is different from that of the emission line scattering region. One common feature in both our data, best seen in SDSSJ1652+1728E, as well as many SNe (Wang & Wheeler 2008), is the presence of loops in the q/u plane, where both the degree of polarization and the polarization position angle vary across the emission line, representing a large physical deviation from axial symmetry. Possible explanations for loops in the q/u plane include an overall asymmetry to the scattering structure, an additional expanding shell with a different geometry, or the breakup of an axially symmetric scattering structure into clumps (Kasen et al. 2003; Wang & Wheeler 2008). In some of our objects, the presence of such a chaotic structure may smear out loops in the q/u plane.

Loops in the q/u plane as a function of wavelength across emission lines has been widely observed in AGN. Smith et al. (1995)

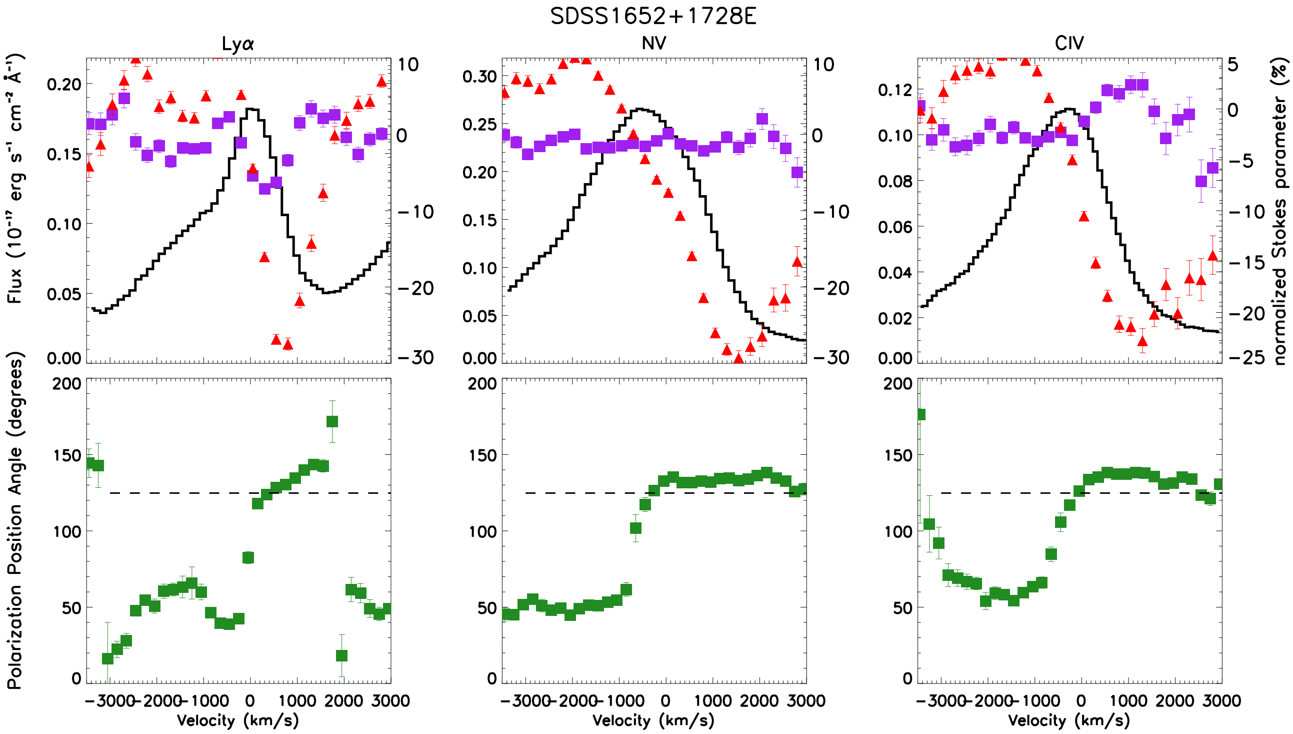

Figure 3. LRISp spectrum of SDSSJ1652+1728E over the emission lines of Ly α, C IV, and N V in velocity space ($\pm$3000 km s^{-1}). A similar figure for the remaining four objects can be found in the Appendix, Fig. A2. We plot the total flux of the line (black histogram) as well as the normalized Stokes parameters q and u in percent (purple square and red triangular points) in bins of 200 km s^{-1} as well as the polarization position angle (green square points) in similar bins below. Finally, the average polarization position angle from the continuum bins as a black dotted line to show where the polarization position angle matches this average value as a function of velocity.

argued that structure in the polarization fraction of the emission lines in Mrk 231 requires several scattering components. Smith et al. (2000) further argued that structure in the polarization fraction and polarization position angle across broad emission lines, coupled with larger values of polarization in the continuum than the emission lines, implies that the BLR of the 2MASS quasars contains multiple scattering components. In contrast, Young (2000), Smith et al. (2005), and Young et al. (2007) argued that such swings in the polarization position angle were due to emission and scattering by an equatorial disc wind that is visible in type 1 quasars but is overwhelmed by polar scattering signatures in type 2 quasars. Typically, however, polarization positions angles changed by only a few to tens of degrees.

The extreme (close to 90°) rotation in the polarization position angle in our objects as a function of velocity within the emission lines implies dramatic changes in the scattering geometry as a function of velocity. The linear features in the q/u plane may be successfully explained by axisymmetric models, which we discuss in the next section. In contrast, loops in the q/u plane imply deviations from axisymmetry, which we do not attempt to model here.

4 DISCUSSION

Several trends are visible in our observations as noted in Section 3:

(i) polarization reaching >10 per cent in the continuum for three of five sources;

(ii) a ratio of emission line polarization to continuum polarization that is <1 for all sources, especially ERQs;

(iii) a change in the polarization position angle across emission lines of $\sim\pi/2$ radians, with the redshifted line emission at the same position angle as the continuum.

4.1 Proposed model

To model these trends, we consider models with a number of ingredients. Polarimetry models include both an emission and scattering region (though they can be coincident), which can be either stationary or have some velocity. In addition, we can vary the type of scatterer and scattering mechanism. For example, the classical model that explains the spectropolarimetry of obscured quasars is that of a point-like emitting region with a conical scattering region defined by the opening angle of the torus (Miller et al. 1991).

Combining all of these considerations, we constructed a model of the emission, scattering, and resulting polarization expected for simple geometries and polarization mechanisms. We find that the model with the best fit to our data is a polar emission region (expanding emission within a filled cone) which is scattered by dust in an equatorial outflow (see Fig. 5 and Veilleux et al. 2016). The full details of this model will be described in Zakamska & Alexandroff (in preparation). While there are certainly more complicated geometries that would reproduce all our results, this model has the advantage of being straightforward and physically motivated.

There is both observational evidence and extensive theoretical work to support an equatorial, dusty outflow from the AGN torus that is supported by radiation pressure (e.g. Wills et al. 1992; Elitzur & Shlosman 2006; Chan & Krolik 2016; Veilleux et al. 2016; Elvis 2017). If the AGN is near or super-Eddington, the creation of a geometrically thick accretion flow also produces polar radiation driven

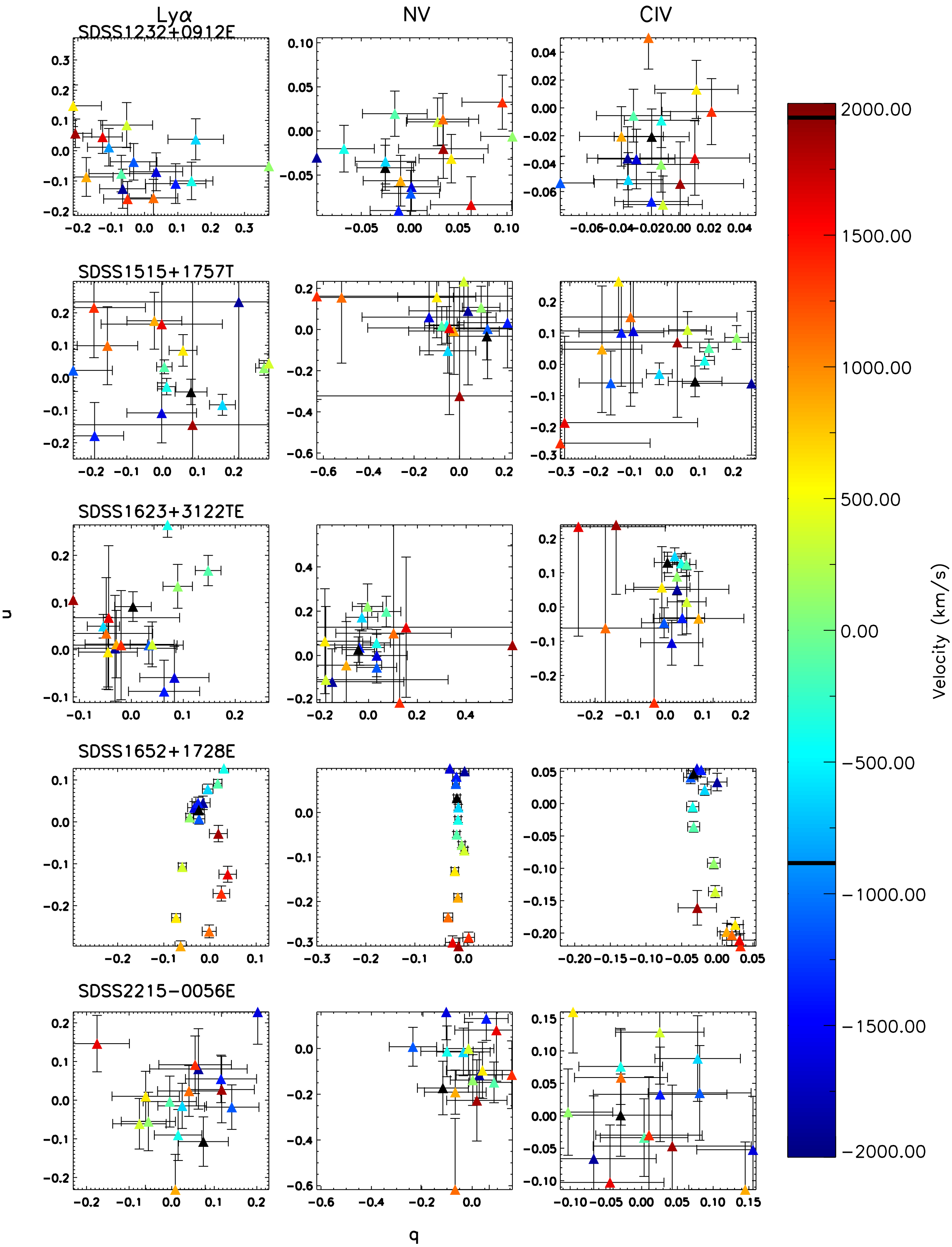

Figure 4. Normalized Stokes parameters q and u for each of the key emission lines in our targets. Each point represents a 250 km s^{-1} bin. We show over ±2000 km s^{-1} in velocity space with the colour scale. In SDSSJ1652+1728E, there is a loop in q versus u space. For the other objects, a potential loop can be identified by a gradient in the colour (velocity) across the q/u plane.

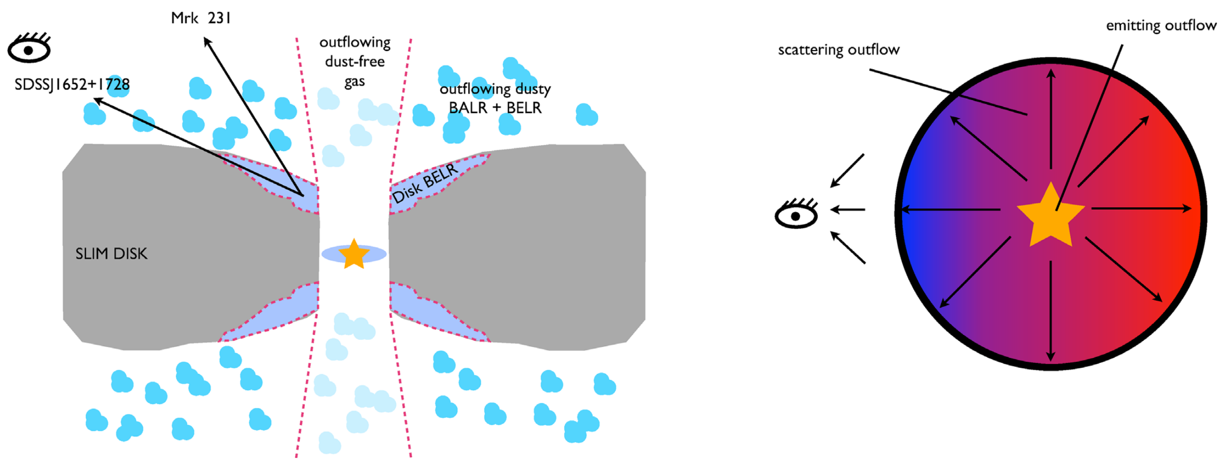

Figure 5. Our preferred model for SDSSJ1652+1728 is adapted from Veilleux et al.(2016). It combines a polar outflow that produces the emission lines with a dusty equatorial wind where the scattering occurs. Left-hand panel: Side-on view of the inner ∼10 pc of our model (not to scale). The inner accretion disc ($\lesssim$0.01 pc) is responsible for the X-ray emission and is surrounded by a geometrically thick accretion disc ('slim disc'), which, for a near- or super-Eddington quasar, produces narrow funnels that drive a polar wind. This polar wind is comprised of both dust-free outflowing gas, responsible for X-ray absorption, as well as dusty clouds that produce FeLoBAL absorption signatures and the blueshifted FUV emission lines of Ly α and C IV. The extended accretion disc is the source of the UV and optical continuum emission as well as the Balmer lines (seen through the screen of the outflowing dusty BALR). Mrk 231 is constrained to have a jet angle of $\theta_{\rm max} = 25.6^{\circ}{}^{+3.2^{\circ}}_{-2.2^{\circ}}$ from radio observations (Reynolds et al. 2013). This means that the scattered light, though still significant, is unpolarized in the observer's line of sight due to geometric cancellation. In contrast, SDSSJ1652+1728 is seen at a larger angle to the jet or polar axis as inferred from the mean SED of ERQs (see Section 4.1 for further discussion). The increased column density of obscuration suppresses the FeLoBAL features while the more edge-on sight line reduces geometric cancellation of the polarization signature. Though the original cartoon from Veilleux et al. (2016) contains a radio jet, we omit this as it is not the subject of this work. Right-hand panel: The same model as viewed from above (looking along the polar axis). Here, we show how the kinematic features in the polarized emission-line regions are created by the blue- and red-shifted scattering emission, respectively. The viewer (eye on the left) sees blue-shifted emission coming towards them and scattered off of clouds moving towards the observer. In contrast, the redshifted wings of the emission lines are dominated by scattering off the 'sides of the outflow (from the observer's perspective). Emission from the back of the cone is largely suppressed in polarization because the scattering efficiency is low at angles $\gtrsim 90^{\circ}$, though this emission does contribute to the overall redshift of polarized emission lines compared to the unpolarized emission lines. These features combined produce the 90°rotation in the polarization position angle across the emission lines.

outflows (e.g. Abramowicz et al. 1988; McKinney, Dai & Avara 2015; Sądowski et al. 2015). We adapt the cartoon of Veilleux et al. (2016), who model Mrk 231 with a slim disc responsible for the continuum emission. The broad emission line region (BELR) is composed of a polar region, an extended accretion disc atmosphere, and the disc itself (see Veilleux et al. 2016, fig. 8 and our Fig. 5), whereas the broad absorption line region (BALR) originates only in the polar outflow and disc atmosphere. Using this model, the FeLoBAL features are produced in the BALR, blueshifted far-ultraviolet (FUV) emission lines are produced in the outflowing BELR, and the optical and NUV emission lines are produced in the disc BELR. We find that some of the features of this model reproduce our spectropolarimetry results well. In particular, when the FUV lines are produced in the polar region and then are scattered by a dusty, ionized equatorial outflow, the puzzling kinematics of the polarized emission lines can be reproduced.

The main difference between Mrk 231 and our objects (ERQs and type 2s) is that our viewing angle is closer to edge-on than the ∼25°polar viewing angle inferred for Mrk 231 from radio observations (Reynolds et al. 2013). We make this conclusion on the basis of the shape of the spectral energy distributions (SEDs) of our sources (Zakamska et al. 2016; Hamann et al. 2017): As a function of wavelength, ERQ SEDs do not rise until 1–2 μm, whereas Mrk 231 is essentially unobscured at red wavelengths in the optical, and the steep rise of the Mrk 231 SED occurs at ∼3000 Å. Therefore, the net line-of-sight column density of obscuration is ∼10 times higher in ERQs than in Mrk 231, implying the more edge-on viewing angle. For an small magellanic cloud (SMC) dust curve (Weingartner & Draine 2001; Draine 2003) in the 'screen of cold dust' approximation, the Mrk 231 rise would correspond to $A_V \simeq 0.3$ mag, and the 1 − 2-μm rise for ERQs would correspond to $A_V \simeq 5$ mag.

The difference in viewing angle could explain why Mrk 231 exhibits low levels of FUV polarization. At the viewing angle of Mrk 231, the scattering region becomes nearly symmetric and thus geometric cancellation would dilute the polarization fraction (similar polarization fractions with opposite scattering angles will combine to produce a lower total polarization fraction) though the scattered flux is still high. In contrast, for the nearly edge-on objects in our sample, the equatorial scattering region is extended in the plane of the sky.

In subsequent sections, we explore how this model matches the observational trends noted in our data. Section 4.2 explains how this model matches our continuum polarization results while Section 4.3 shows how this model reproduces the observed line polarization. Finally, in Section 4.4, we demonstrate that resonant scattering does not have a significant impact on our preferred model.

4.2 Continuum polarization and scattering geometry

While scattering off of dust or electrons is the most likely source of polarization in AGN, observed especially at the high levels in our objects, without some understanding from the imaging of the scales on which polarization occurs, it is difficult to distinguish between the two. For objects where the scattering cone is visible on ∼kpc scales (Dey et al. 1996; Kishimoto et al. 2001; Zakamska et al. 2005), the dominant scatterer is likely dust. In these cases, the required gas mass for electron scattering is likely prohibitively high though it is not always possible to completely rule out electron scattering. In contrast, on circumnuclear scales, the polarization of NGC 1068 is wavelength-independent from the X-ray to the optical, and is therefore likely due to electron scattering (Miller et al. 1991).

The high infrared-to-optical ratios and multiple features of the rest-frame optical spectra of our objects (Alexandroff et al. 2013; Ross et al. 2015; Zakamska et al. 2016; Hamann et al. 2017) indicate that they are obscured. We also know that the observed UV continuum of our objects is dominated by scattered light, because the net continuum polarization is so high that it cannot be appreciably diluted by the direct (unpolarized) light of the quasar. Therefore, scattering must be happening primarily on scales greater than obscuration scales, which, in turn, must be larger than the dust sublimation region (defined by the radius, $r_{\rm dust}$; Barvainis 1987, equation 5):

$$r_{\rm dust} = 1.3\left(\frac{L_{\rm UV}}{10^{46}{\rm erg\,s^{-1}}}\right)^{1/2}\left(\frac{T}{1500{\rm K}}\right)^{-2.8}{\rm pc}. \quad (1)$$

Here, $L_{\rm UV}$ is the UV luminosity and T is the dust sublimation temperature. In the case of our extremely luminous sources ($L_{\rm UV} \approx$ a few $\times$ 10^{47} erg s^{-1}), the sublimation scales might reach a few to 10 pc. In ERQs, this is quite consistent with the scales of obscuration inferred from X-ray observations (Goulding et al. 2018).

For a normal dust-to-gas ratio, the cross-section of dust scattering is two orders of magnitude higher than the electron scattering cross-section (Draine 2003), therefore since scattering must be happening outside of the dust sublimation zone, the presence of dust implies that dust scattering dominates our scattered light. In our proposed model, therefore, the dust scattering occurs somewhere in the BELR/BALR region (see Fig. 5).

The scattering efficiency, the ratio of scattered flux to the flux that would have been observed directly in the absence of obscuration, is defined as

$$\epsilon = \frac{{\rm d}\sigma}{{\rm d}\Omega}\Delta\Omega\int n_{\rm H}(r){\rm d}r. \quad (2)$$

Here, ${\rm d}\sigma/{\rm d}\Omega$ is the cross-section of scattering per unit hydrogen atom as calculated in Draine (2003), $\Delta\Omega$ is the solid angle covered by the scatterer as seen from the emitter, and $\int n_{\rm H}(r){\rm d}r$ is the column density of hydrogen associated with the scattering region. For a constant velocity outflow, $n_{\rm H}(r) \propto 1/r^2$, and therefore this integral is weighted towards the smallest unobscured sizes, so it is $\sim n_{\rm H,\,max}d_{\rm min}$. We take a fiducial value of $\epsilon = 3$ per cent, which is obtained by extrapolating the IR emission of ERQs using a type 1 quasar SED (Richards et al. 2006) towards UV wavelengths to see what fraction of this estimated intrinsic emission is observed (see fig. 16 of Zakamska et al. 2016 as well as fig. 8 of Hamann et al. 2017). We take $\Delta\Omega = \frac{4\pi}{3}$ and 90° scattering by SMC dust with ${\rm d}\sigma/{\rm d}\Omega \simeq 4 \times 10^{-24}$ cm^2/H/sr at 1500 Å (Draine 2003). We arrive at the constraint in the density-scale plane in Fig. 6, implying hydrogen densities for scattering material of the order of 10–100 cm^{-3}.

If this scattering region were too dusty, then no emission from the quasar could escape at all. Therefore, we need to verify that our derived densities and sizes are compatible with the escape of radiation from the quasar in order to be available for scattering into our line of sight. We use equation 3 to find the optical depth to dust extinction through the scattering region:

$$\tau = C_{\rm ext}\int n_{\rm H}{\rm d}r = \frac{\epsilon C_{\rm ext}}{\Delta\Omega{\rm d}\sigma/{\rm d}\Omega}, \quad (3)$$

where $C_{\rm ext} = 2.9 \times 10^{-22}$ cm^2/H is the total cross-section for extinction (Weingartner & Draine 2001). With our fiducial values, $\tau \simeq 0.5$, and is therefore just right: A quasar viewed through the

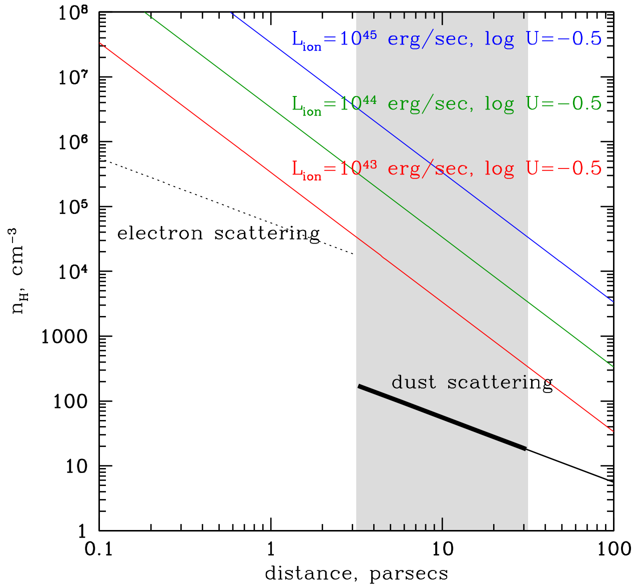

Figure 6. The scattering efficiency and ionization parameter allow us to place constraints on the size of the scattering region and the density of scattering material. Assuming a scattering efficiency of 3 per cent and following from equation 2, the black lines show the range of densities for reasonable distances to the dust (solid) or electron (dotted) scattering regions, respectively. The coloured lines in the upper right show the limits on the density placed at the same distances based on our assumptions of the quasar ionizing luminosity and ionization parameter (see equation 4). Our preferred regime is the grey region that covers dust scattering at scales 3–30 pc (around the dust sublimation radius), though we are not able to place strong limits on the actual ionizing luminosity available from our quasars, which is, additionally, likely suppressed by extinction. It is clear from this figure that the two limits, derived from the scattering efficiency and the ionization parameter, are incompatible. We hypothesize that this is the case because while the line emission occurs in dense clouds located in the quasar BELR, the scattering occurs on similar scales but in the less dense medium surrounding these clouds.

BELR/BALR would be reddened, as is Mrk 231, but not completely extinguished. We also see from this expression that the scattering efficiency, ϵ, cannot be much greater than our fiducial value, because otherwise the extinction becomes prohibitively high. Therefore, we conclude that our observed scattered component cannot be appreciably obscured, either by diffuse or by patchy material.

Assuming an SMC-like dust distribution, the theoretically achievable maximum polarization fraction at 1800 Å is ∼14.7 per cent for a scattering angle of 90° and the polarization fraction continues to rise towards the blue (Draine 2003). Thus, some of our targets display such high levels of polarization in the continuum that they come close to reaching this theoretically achievable limit, and the geometric cancellation of polarization means that to achieve the observed 15 per cent polarization level, the intrinsic polarization level of each scattering must be even higher. We know dust can be an efficient polarizer depending on the size distribution of the dust as compared to the wavelength of the scattered light (Weingartner & Draine 2001). Thus, achieving the observed polarization fraction in our sources might require some adjustments to the dust size distribution compared to pre-existing models. Adjustments from the Draine (2003) models may also be necessary to explain any increase in the polarization fraction of our objects towards redder wavelengths (the opposite of current model predictions). It is also not possible at this time to rule out a wavelength-dependent unpolarized component that dilutes the polarization as the cause of any wavelength-dependent polarization signatures in our continuum data.

4.3 Line polarization

In low-redshift type 2 quasars, scattering occurs on a wide range of scales, reaching several kpc (Hines et al. 1999; Zakamska et al. 2005, 2006; Schmidt et al. 2007; Obied et al. 2016), comparable to the scales on which optical forbidden lines such as [O III] are produced. The co-spatial distribution of the line-emitting gas and of the scattering medium leads to a geometric cancellation of the polarization of the emission lines and to mixing of direct (unpolarized) emission with scattered light, resulting in the observed low fractional polarization of the narrow emission-line region (Stockman et al. 1981; Glenn et al. 1994; Goodrich & Miller 1995; Tran 1995).

In our objects, we observe a lower net polarization of the UV emission lines than the continuum. By analogy to the suppression of polarization of the narrow-line region of type 2 quasars, we hypothesize that the UV emission lines arise on scales similar to those that dominate scattering. In the cartoon shown in Fig. 5, the low fractional polarization of the emission lines would be achieved if the lines are produced either in the dusty BELR/BALR or in the dust-free cone at scales similar to or greater than the scales of the dusty BELR/BALR. There is also empirical evidence (Czerny & Hryniewicz 2011) and emission line calculations (Netzer & Laor 1993) that suggest the BLR and inner edge of the obscuring material should exist on similar scales. Finally, in a recent paper, Baskin & Laor (2018) present detailed calculations of the geometry of both the dust-free and the dusty BELR.

In the simple case of a spherical emitting region of radius R and scattering region of radius D, Cassinelli, Nordsieck & Murison (1987) show that the polarization is reduced by a factor of $[1 - (R/D)^2]^{1/2}$ relative to an emitting point source. If we assume that the continuum emitting region is a point source, and it is roughly $\sim$3 times more polarized than the emission line region, this implies that the emission line region is 94 per cent the size of the scattering region, confirming that the emission line region and scattering regions extend to similar scales.

What constraints on the physical conditions do we get from requiring that continuum scattering and UV emission line production occur on similar scales? The ionization parameter is

$$U = \frac{L_{\rm ion}}{4\pi r^2 \phi n_{\rm e} c}. \quad (4)$$

Here, $L_{\rm ion}$ is the luminosity of the ionizing radiation, $\phi = 13.6$ eV is the threshold energy of the ionizing photons, and $n_{\rm e} \simeq (1 - 1.2) \times n_{\rm H}$ is the electron density that depends slightly on whether helium is fully ionized. As a fiducial value of the ionization parameter in the C IV-emitting region, we use $\log U = -0.5$ from Rodríguez Hidalgo, Hamann & Hall (2011). As discussed in Section 3.3, emission lines that we see in the rest-frame UV spectra originate on the scales similar to scattering – i.e. on scales that are larger than the dust sublimation distance. Therefore, we consider the possibility that the line-emitting clouds are subjected to an ionizing continuum that is strongly suppressed by dust extinction. We plot the resulting relationship between n_H and r in Fig. 6 for various values of $L_{\rm ion}$.

It is clear from Fig. 6 that if emission lines are produced on spatial scales that are similar to those of scattering, then either a strong suppression of the ionizing continuum or strong clumping of the emission-line gas, or both, is required to produce the observed ionization parameter. We will model the UV emission lines of ERQs in a forthcoming photo-ionization analysis of the emission line ratios (Hamann et al., in preparation). In the meanwhile, our qualitative model is that the emission lines are produced in high density clouds either in the joint BELR/BALR or in the dust-free zone. These clouds are ionization-bounded and therefore are by definition optically thick to ionizing radiation, so only the compact surfaces of these clouds will be able to scatter continuum emission in the dusty zone (scattering is much weaker in the dust-free zone and is unlikely to dominate). Thus, scattering is dominated by a lower density, volume-filling component of the BELR/BALR gas. This allows us to reconcile the densities implied by the scattering efficiency and by the ionization parameter (see Fig. 6).

The biggest success of our model in Fig. 5 is that it naturally explains the change in the polarization fraction and position angle as a function of velocity in the FUV emission lines. The blue-shifted line emission we see in our objects is from the near-side of the equatorial outflow, which gives it the observed velocity shift (see the right-hand panel of Fig. 5). In contrast, the observed redshifted emission is dominated not by the back of the outflow (this emission is suppressed because dust back scattering is inefficient) but instead from the sides of the equatorial outflow, which are moving away from the observer and thus produce redshifted scattered emission. This results in the swing in polarization position angle as a function of velocity in the emission lines as the two scattering regions are roughly perpendicular to each other as seen in the plane of the sky. As a result, the polarization position angle transitions as a function of velocity from being dominated by the near-side of the equatorial outflow in the blue to the sides of the outflow in the red. This also explains the overall redshift in emission line features seen in polarized light as the net redshift of the scattered line is due to the redshift of the scatterer relative to the emitter.

Finally, in our model we expect the polarization fraction of the blue wing to be low due to the low polarization efficiency of forward scattering. This is indeed clearly seen in the data. In Fig. 2, the dominant polarization signal is represented by the u values of polarization. The absolute value of $|u|$ reaches 30 per cent at $v \simeq +1500\,{\rm km\,s^{-1}}$ and only 5 per cent on the blue end at $v < 0$. This decline of polarization on the blue wing is another major success of our model.

Smith et al. (2004) suggested a similar model of the torus with both polar and equatorial scattering regions to explain the range of properties observed in low redshift Seyfert 1s and 2s. The polar scatterer extends beyond the torus and may be outflowing while the equatorial scatterer lies within the torus, and is described by Young (2000) as a rotating disc wind. Other differences between our model and the Young (2000) model include the specific emission lines: They consider Balmer lines, which in our cartoon are produced in a more extended region of the disc than the FUV lines, which we focus on. Furthermore, in type 1 objects, there is dilution of the scattered light by the direct unpolarized continuum, which may explain the much lower values of polarization and position angle swings achieved in Seyfert 1s. But the main difference is that Young (2000) explains the rotation in the polarization position angle using a rotating disc wind, where rotation might be difficult to maintain dynamically. In contrast, in our model, the polarization position angle swing is achieved naturally by the geometric projection effects, with the blueshifted scattered emission and the redshifted scattered emission having different orientations in projection on the plane of the sky.

4.4 Resonant scattering?

In addition to scattering by either electrons or dust grains, resonant scattering is a possible mechanism for the polarization observed in the emission lines of our objects. Permitted electric dipole transitions in an anisotropic radiation field can produce linearly polarized emission, and thus resonantly polarized scattering becomes an important mechanism either if the emission line source region is not spherically symmetric or if radiation, either from an emission line or the continuum region, is Doppler-shifted into resonance with a permitted transition and is incident on a gas cloud (Lee & Blandford 1997). For a single $\Delta J = 0 - 1$ scattering viewed at 90°, the polarization reaches 100 per cent (Hamilton 1947). However, the resonant scattering in AGNs might involve multiple scatterings, and if the optical depth to scattering is high enough the net expected polarization signal is low. Lee (1994) showed that standard emission-line clouds emit almost completely unpolarized line radiation unless the optical depth is $\tau \lesssim 1$, which is usually only the case for the semi-forbidden C III] λ1909 transition. For reflection off of nearby clouds to contribute significantly to the polarized line emission, the optical depth must be in a specific regime where only a small number of reflections occur. Lee & Blandford (1997) determine that this happens at a column density of $N \sim 10^{17}$ cm^{-2} for a single reflection, which is several six orders of magnitude smaller than the regime where dust ($N \sim 10^{21}$ cm^{-2}) or electron scattering have a significant effect ($N \sim 10^{23}$ cm^{-2}).

We can calculate the expected ratio of the optical depth of resonant scattering compared to the optical depth to dust scattering. The optical depth to dust scattering, $\tau_{\rm dust}$, is given by

$$\tau_{\rm dust} = N_{\rm H} \times C_{\rm ext,H}, \quad (5)$$

assuming a constant number density of dust grains along the line of sight. Here, $N_{\rm H}$ is the column density of hydrogen nucleons and $C_{\rm ext,\,H}$ is the extinction cross section of the dust per hydrogen nucleon, taken to be 3.768×10^{-22} cm^2/H for an SMC-like dust distribution at 1200 Å from Draine (2003). Similarly, the optical depth to resonant scattering, $\tau_{\rm res}$, is given by

$$\tau_{\rm res} = N_{\rm H} \times \frac{m_{\rm C}}{m_{\rm H}} \frac{\Delta v}{v_{\rm wind}} \sigma_{\rm res}, \quad (6)$$

where $\frac{m_{\rm C}}{m_{\rm H}} \simeq 1.0 \times 10^{-3}$ is the mass ratio of C IV to H nucleons, which we estimate based on the assumption that the number ratio of carbon to hydrogen in the interstellar medium is solar, $\frac{\log N_{\rm H}}{\log N_{\rm C}} = 3.57$ (Grevesse et al. 2010), and ~30 per cent of carbon is triply ionized (D. Proga, private communication). Next, $\frac{\Delta v}{v_{\rm wind}} \approx 0.1$ is the fraction of photons that lie within a thermal width of the resonance frequency given an estimate of the outflow velocity of $v_{\rm wind} \approx 3000$ km s^{-1} and the gas temperature $T \approx 15\,000$ K based on the assumption of photo-electric temperature balance for C IV. Finally, the cross section for resonant scattering is taken to be $\sim 1.0 \times 10^{-17}$ cm^2 for a single scattering event as taken from Lee, Blandford & Western (1994). Combining these quantities gives us a rough estimate for the ratio of the dust scattering to resonant scattering optical depth of $\frac{\tau_{\rm res}}{\tau_{\rm dust}} \approx 0.3$, implying that resonant scattering in the emission lines of our objects is likely present but at most enhances the polarization fraction by ~30 per cent. We thus conclude that continuum dust scattering is the dominant scattering mechanism both for the continuum and the emission lines.

5 CONCLUSIONS

We have obtained rest-frame UV spectropolarimetry for five $z \sim 2.5$ obscured and highly reddened quasars using LRIS in polarimetry mode on Keck. Our type 2 targets are classically selected, narrow-line objects (Alexandroff et al. 2013). ERQs are colour-selected and show signs of extreme outflow activity in their rest-frame optical spectra (Ross et al. 2015; Zakamska et al. 2016; Hamann et al. 2017). Although our initial expectations were that narrow line-selected type 2 quasars should have a more axisymmetric scattering region and that they should therefore be more highly polarized than the ERQs, we find (in this admittedly small sample) no systematic trends between the optical and UV 'type' and the levels of continuum polarization.

We do see several interesting trends in our polarization data, which are as follows:

(i) We find high levels of polarization in the continuum, higher than 10 per cent in three of our sources.

(ii) We find lower levels of polarization in emission lines with a ratio of emission line polarization/continuum polarization between 0.3 and 0.8.

(iii) Intriguingly, we see a rotation of almost exactly 90°in the polarization position angle across all strong emission lines, Ly α, C IV, and N V.

(iv) The polarization position angle of the continuum matches the polarization position angle in the redshifted wings of the emission lines.

To explain our data, we prefer a model in which an equatorial dusty disc wind scatters both continuum emission from the disc and line emission from a polar outflow. This model is physically motivated and appears to match the main features of our observations. The high polarization fraction can be explained by dust scattering though it may require a few adjustments to typical dust models. Assuming the emission line region and dusty scattering region exist on similar scales that are larger than the continuum emission region produces the lower polarization fraction observed in the emission lines of our objects. Finally, this model allows for different outflow components to dominate in the continuum and the red wavelengths of emission lines compared to the blue wavelengths of emission lines and thus produces a 90° rotation in the polarization position angle as a function of wavelength across the emission lines as observed.

Absent high-resolution imaging, spectropolarimetry is an important tool to understand the scattering geometry of our high redshift obscured and reddened quasars and can be an important piece of information to evaluate different proposed models of quasar geometry on small scales near the black hole. While polarimetry measurements remain difficult, searching for a small signal in already faint objects, it appears that obscured and red quasars at redshifts where host galaxy contamination is small often show polarization fractions in excess of 10 per cent, which makes the outlook for future studies more optimistic. Future spectropolarimetric studies will allow us a window into the potential launching mechanism for galaxy-scale quasar winds that are a necessary ingredient for quasar feedback.

ACKNOWLEDGEMENTS

The data presented herein were obtained at the W.M. Keck Observatory, which is operated as a scientific partnership among the California Institute of Technology, the University of California, and the

National Aeronautics and Space Administration. The Observatory was made possible by the generous financial support of the W.M. Keck Foundation. The authors wish to recognize and acknowledge the very significant cultural role and reverence that the summit of Maunakea has always had within the indigenous Hawaiian community. We are most fortunate to have the opportunity to conduct observations from this mountain.

Funding for SDSS-III has been provided by the Alfred P. Sloan Foundation, the Participating Institutions, the National Science Foundation, and the U.S. Department of Energy Office of Science. The SDSS-III web site is http://www.sdss3.org/.

SDSS-III is managed by the Astrophysical Research Consortium for the Participating Institutions of the SDSS-III Collaboration including the University of Arizona, the Brazillian Participation Group, Brookhaven National Laboratory, Carnegie Mellon University, University of Florida, the French Participation Group, the German Participipartion Group, Harvard University, the Instituto de Astrofisica de Canarias, the Michigan State/Notre Dame/JINA Participation Group, Johns Hopkins University, Lawrence Berkeley National Laboratory, Max Planck Institute for Astrophysics, Max Planck Institute for Extraterrestrial Physics, New Mexico State University, New York University, Ohio State University, Pennsylvania State University, University of Portsmouth, Princeton University, the Spanish Participation Group, University of Tokyo, University of Utah, Vanderbilt University, University of Virginia, University of Washington, Yale University.

This research has made use of the NASA/IPAC Infrared Science Archive, which is operated by the Jet Propulsion Laboratory, California Institute of Technology, under contract with the National Aeronautics and Space Administration

We would like to thank the referee for many helpful comments and suggestions, the inclusion of which helped to improve our paper. RMA would like to acknowledge the assistance of C. Steidel, A. Strom, D. Perley, and H. Tran during observations at Keck I and the assistance of M. Kassis on the evening of LRISp observations. RMA would also like to thank D. Neufeld for useful conversations and S. Veilleux for allowing us to adapt fig. 8 of Veilleux et al. (2016). NLZ would like to acknowledge the remote observing support of Yale University.

RMA was supported in part by NASA JPL grant 1520456. Support for this work was provided in part by the National Aeronautics and Space Administration through Chandra Award Number GO6-17100X issued by the Chandra X-ray Observatory Center, which is operated by the Smithsonian Astrophysical Observatory for and on behalf of the National Aeronautics Space Administration under contract NAS8-03060. NLZ acknowledges support by the Catalyst award of the Johns Hopkins University. Research by AJB is supported in part by NSF grant AST-1412693.

REFERENCES

Abramowicz M. A., Czerny B., Lasota J. P., Szuszkiewicz E., 1988, ApJ, 332, 646
Ahn C. P. et al., 2012, ApJS, 203, 21
Alexandroff R. et al., 2013, MNRAS, 435, 3306
Antonucci R., 1993, ARA&A, 31, 473
Antonucci R. R. J., Miller J. S., 1985, ApJ, 297, 621
Assef R. J. et al., 2016, ApJ, 819, 111
Banerji M., Alaghband-Zadeh S., Hewett P. C., McMahon R. G., 2015, MNRAS, 447, 3368
Barth A. J., Filippenko A. V., Moran E. C., 1999, ApJ, 525, 673
Barvainis R., 1987, ApJ, 320, 537
Baskin A., Laor A., 2018, MNRAS, 474, 1970
Berriman G., Schmidt G. D., West S. C., Stockman H. S., 1990, ApJS, 74, 869
Borguet B., Hutsemékers D., Letawe G., Letawe Y., Magain P., 2008, A&A, 478, 321
Cassinelli J. P., Nordsieck K. H., Murison M. A., 1987, ApJ, 317, 290
Chan C.-H., Krolik J. H., 2016, ApJ, 825, 67
Clemens D. P., Tapia S., 1990, PASP, 102, 179
Czerny B., Hryniewicz K., 2011, A&A, 525, L8
Dawson K. S. et al., 2013, AJ, 145, 10
Dey A., Cimatti A., van Breugel W., Antonucci R., Spinrad H., 1996, ApJ, 465, 157
Donley J. L. et al., 2012, ApJ, 748, 142
Draine B. T., 2003, ApJ, 598, 1017
Eisenhardt P. R. M. et al., 2012, ApJ, 755, 173
Elitzur M., Shlosman I., 2006, ApJ, 648, L101
Elvis M., ApJ, 2017, 847, 56
Glenn J., Schmidt G. D., Foltz C. B., 1994, ApJ, 434, L47
Glikman E. et al., 2012, ApJ, 757, 51
Glikman E. et al., 2013, ApJ, 778, 127
Glikman E., Helfand D. J., White R. L., Becker R. H., Gregg M. D., Lacy M., 2007, ApJ, 667, 673
Glikman E., Simmons B., Mailly M., Schawinski K., Urry C. M., Lacy M., 2015, ApJ, 806, 218
Goodrich R. W., Miller J. S., 1995, ApJ, 448, L73
Goodrich R. W., Cohen M. H., Putney A., 1995, PASP, 107, 179
Goulding A. D. et al., 2018, ApJ, 856, 4
Greene J. E. et al., 2014, ApJ, 788, 91
Grevesse N., Asplund M., Sauval A. J., Scott P., 2010, Ap&SS, 328, 179
Hamann F. et al., 2017, MNRAS, 464, 3431
Hamann F., Kanekar N., Prochaska J. X., Murphy M. T., Ellison S., Malec A. L., Milutinovic N., Ubachs W., 2011, MNRAS, 410, 1957
Hamilton D. R., 1947, ApJ, 106, 457
Hao L. et al., 2005, AJ, 129, 1783
Hines D. C., Schmidt G. D., Smith P. S., Cutri R. M., Low F. J., 1995, ApJ, 450, L1
Hines D. C., Schmidt G. D., Wills B. J., Smith P. S., Sowinski L. G., 1999, ApJ, 512, 145
Hines D. C., Schmidt G. D., Gordon K. D., Smith P. S., Wills B. J., Allen R. G., Sitko M. L., 2001, ApJ, 563, 512
Hoeflich P., Wheeler J. C., Hines D. C., Trammell S. R., 1996, ApJ, 459, 307
Hopkins P. F., Hernquist L., Cox T. J., Di Matteo T., Robertson B., Springel V., 2006, ApJS, 163, 1
Horne K., 1986, PASP, 98, 609
Kasen D. et al., 2003, ApJ, 593, 788
Kauffmann G. et al., 2003, MNRAS, 346, 1055
Khachikian E. Y., Weedman D. W., 1974, ApJ, 192, 581
Kishimoto M., Antonucci R., Cimatti A., Hurt T., Dey A., van Breugel W., Spinrad H., 2001, ApJ, 547, 667
Lee H. W., 1994, MNRAS, 268, 49
Lee H.-W., Blandford R. D., 1997, MNRAS, 288, 19
Lee H.-W., Blandford R. D., Western L., 1994, MNRAS, 267, 303
Mason R. E. et al., 2015, ApJS, 217, 13
McKinney J. C., Dai L., Avara M. J., 2015, MNRAS, 454, L6
Miller J. S., Goodrich R. W., 1990, ApJ, 355, 456
Miller J. S., Robinson L. B., Goodrich R. W., 1988, in Robinson L. B., ed., Instrumentation for Ground-Based Optical Astronomy. Springer-Verlag, New York, NY, p. 157
Miller J. S., Goodrich R. W., Mathews W. G., 1991, ApJ, 378, 47
Netzer H., Laor A., 1993, ApJ, 404, L51
Norman C. et al., 2002, ApJ, 571, 218
Obied G., Zakamska N. L., Wylezalek D., Liu G., 2016, MNRAS, 456, 2861
Oke J. B. et al., 1995, PASP, 107, 375
Reyes R. et al., 2008, AJ, 136, 2373
Reynolds C., Punsly B., O'Dea C. P., Hurley-Walker N., 2013, ApJ, 776, L21
Richards G. T. et al., 2006, ApJS, 166, 470

Rockosi C. et al., 2010, in Proc. SPIEConf. Ser. Vol. 7735, Ground-based and Airborne Instrumentation for Astronomy III. SPIE, Bellingham, p. 77350R
Rodríguez Hidalgo P., Hamann F., Hall P., 2011, MNRAS, 411, 247
Ross N. P. et al., 2015, MNRAS, 453, 3932
Sanders D. B., Soifer B. T., Elias J. H., Madore B. F., Matthews K., Neugebauer G., Scoville N. Z., 1988, ApJ, 325, 74
Schlafly E. F., Finkbeiner D. P., 2011, ApJ, 737, 103
Schlegel D. J., Finkbeiner D. P., Davis M., 1998, ApJ, 500, 525
Schmidt G. D., Elston R., Lupie O. L., 1992, AJ, 104, 1563
Schmidt G. D., Stockman H. S., Smith P. S., 1992, ApJ, 398, L57
Schmidt G. D., Smith P. S., Hines D. C., Tremonti C. A., Low F. J., 2007, ApJ, 666, 784
Serkowski K., Mathewson D. S., Ford V. L., 1975, ApJ, 196, 261
Smith P. S., Schmidt G. D., Allen R. G., Angel J. R. P., 1995, ApJ, 444, 146
Smith P. S., Schmidt G. D., Hines D. C., Cutri R. M., Nelson B. O., 2000, ApJ, 545, L19
Smith P. S., Schmidt G. D., Hines D. C., Cutri R. M., Nelson B. O., 2002, ApJ, 569, 23
Smith P. S., Schmidt G. D., Hines D. C., Foltz C. B., 2003, ApJ, 593, 676
Smith J. E., Robinson A., Alexander D. M., Young S., Axon D. J., Corbett E. A., 2004, MNRAS, 350, 140
Smith J. E., Robinson A., Young S., Axon D. J., Corbett E. A., 2005, MNRAS, 359, 846
Stern D. et al., 2002, ApJ, 568, 71
Stern D. et al., 2005, ApJ, 631, 163
Stockman H. S., Hier R. G., Angel J. R. P., 1981, ApJ, 243, 404
Sądowski A., Narayan R., Tchekhovskoy A., Abarca D., Zhu Y., McKinney J. C., 2015, MNRAS, 447, 49
Tadhunter C., 2005, in Adamson A., Aspin C., Davis C., Fujiyoshi T., eds, ASP Conf. Ser., Vol. 343, Astronomical Polarimetry: Current Status and Future Directions. Astron. Soc. Pac., San Francisco, p. 457
Tran H. D., 1995, ApJ, 440, 597
Tran H. D., Cohen M. H., Goodrich R. W., 1995, AJ, 110, 2597
Treister E. et al., 2009, ApJ, 706, 535
Tsai C.-W. et al., 2015, ApJ, 805, 90
Urrutia T., Becker R. H., White R. L., Glikman E., Lacy M., Hodge J., Gregg M. D., 2009, ApJ, 698, 1095
Urry C. M., Padovani P., 1995, PASP, 107, 803
van Dokkum P. G., 2001, PASP, 113, 1420
Veilleux S., Melendez M., Tripp T. M., Hamann F., Rupke D. S. N., 2016, ApJ, 825, 42
Vernet J., Fosbury R. A. E., Villar-Martín M., Cohen M. H., Cimatti A., di Serego Alighieri S., Goodrich R. W., 2001, A&A, 366, 7
Wang L., Wheeler J. C., 2008, ARA&A, 46, 433
Wang L., Howell D. A., Höflich P., Wheeler J. C., 2001, ApJ, 550, 1030
Weingartner J. C., Draine B. T., 2001, ApJ, 548, 296
Wills B. J., Wills D., Evans N. J., II, Natta A., Thompson K. L., Breger M., Sitko M. L., 1992, ApJ, 400, 96
Wright E. L. et al., 2010, AJ, 140, 1868
Wu J. et al., 2012, ApJ, 756, 96
Yèche C. et al., 2010, A&A, 523, A14
Young S., 2000, MNRAS, 312, 567
Young S., Axon D. J., Robinson A., Hough J. H., Smith J. E., 2007, Nature, 450, 74
Yuan S., Strauss M. A., Zakamska N. L., 2016, MNRAS, 462, 1603
Zakamska N. L. et al., 2003, AJ, 126, 2125
Zakamska N. L. et al., 2005, AJ, 129, 1212
Zakamska N. L. et al., 2006, AJ, 132, 1496
Zakamska N. L. et al., 2016, MNRAS, 459, 3144
Zakamska N. L., Greene J. E., 2014, MNRAS, 442, 784
Zubko V. G., Laor A., 2000, ApJS, 128, 245

APPENDIX: ADDITIONAL FIGURES

These figures correspond to Figs 2 and 3 in the main paper but show data for the additional four objects not shown in the main paper.

This paper has been typeset from a TEX/LATEX file prepared by the author.

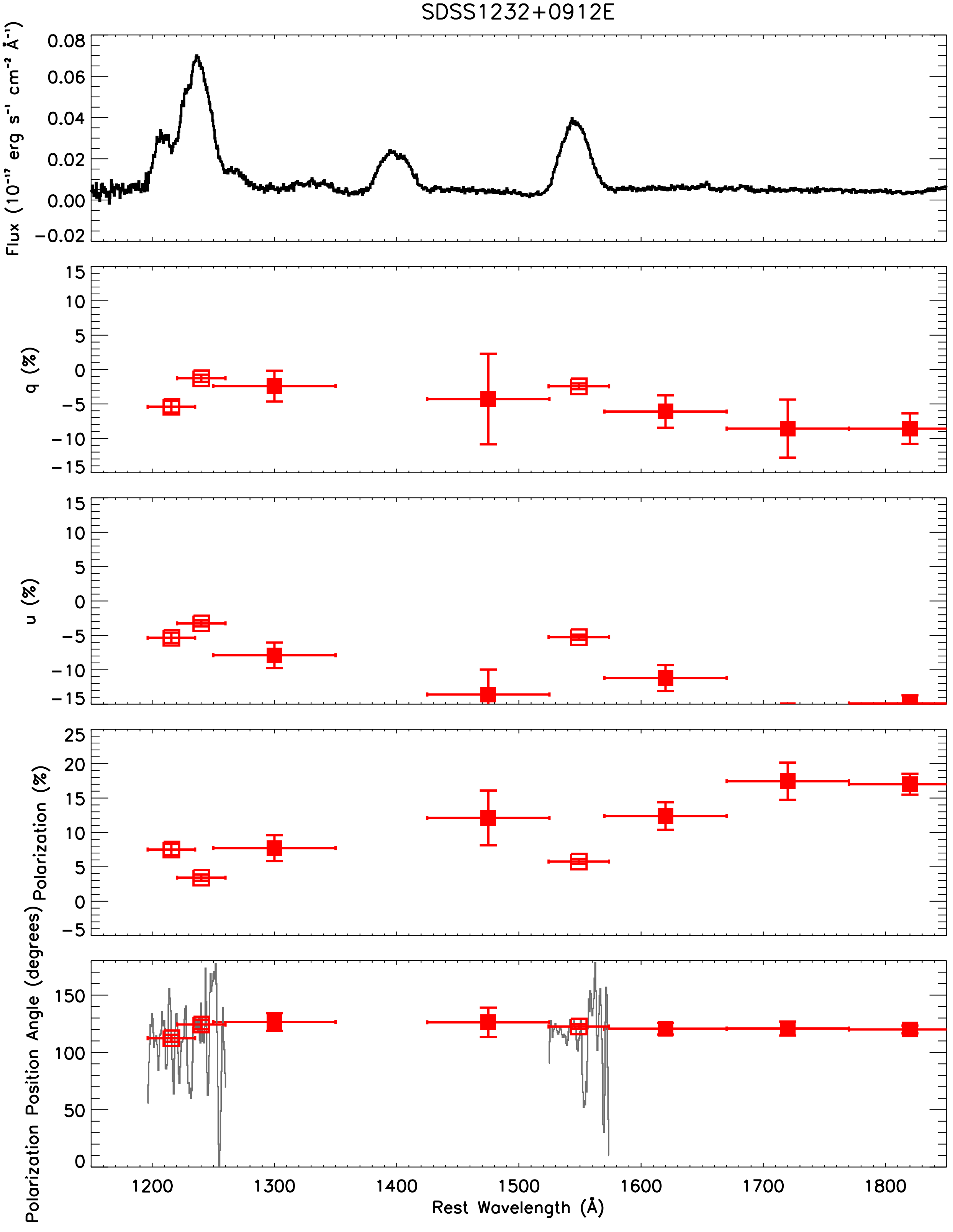

Figure A1. LRISp spectra of our remaining targets (see Fig. 2).

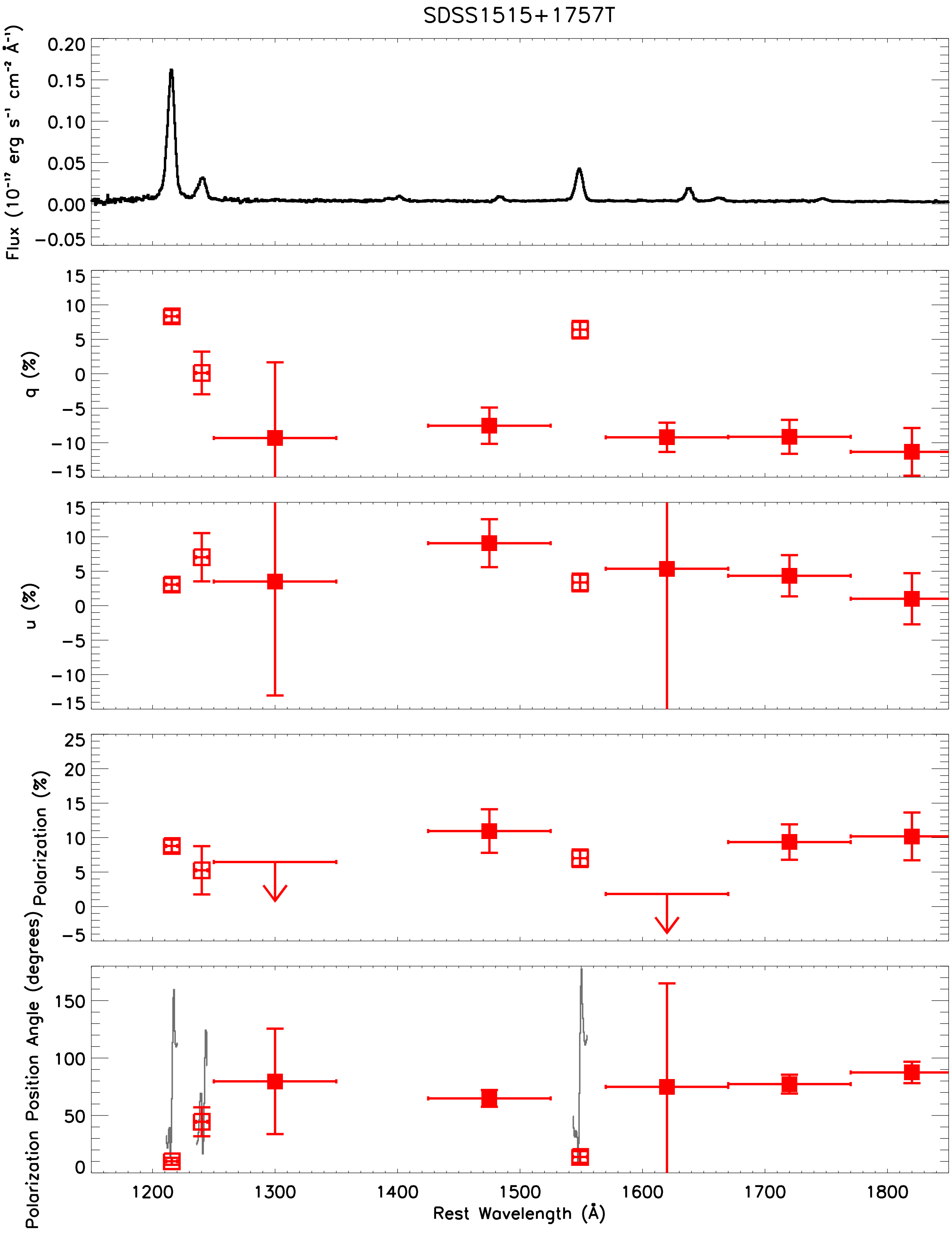

Figure A1. cont.

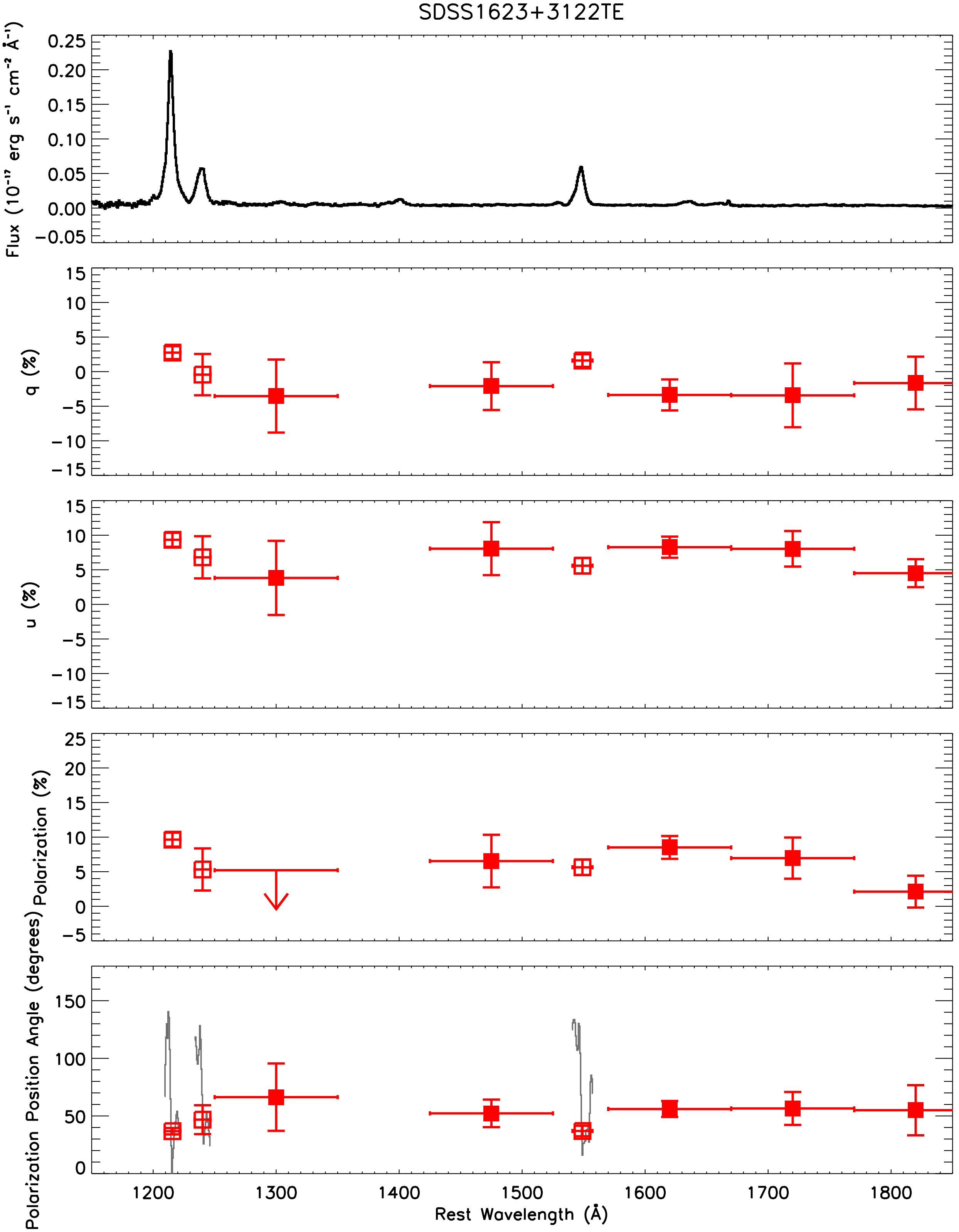

Figure A1. cont.

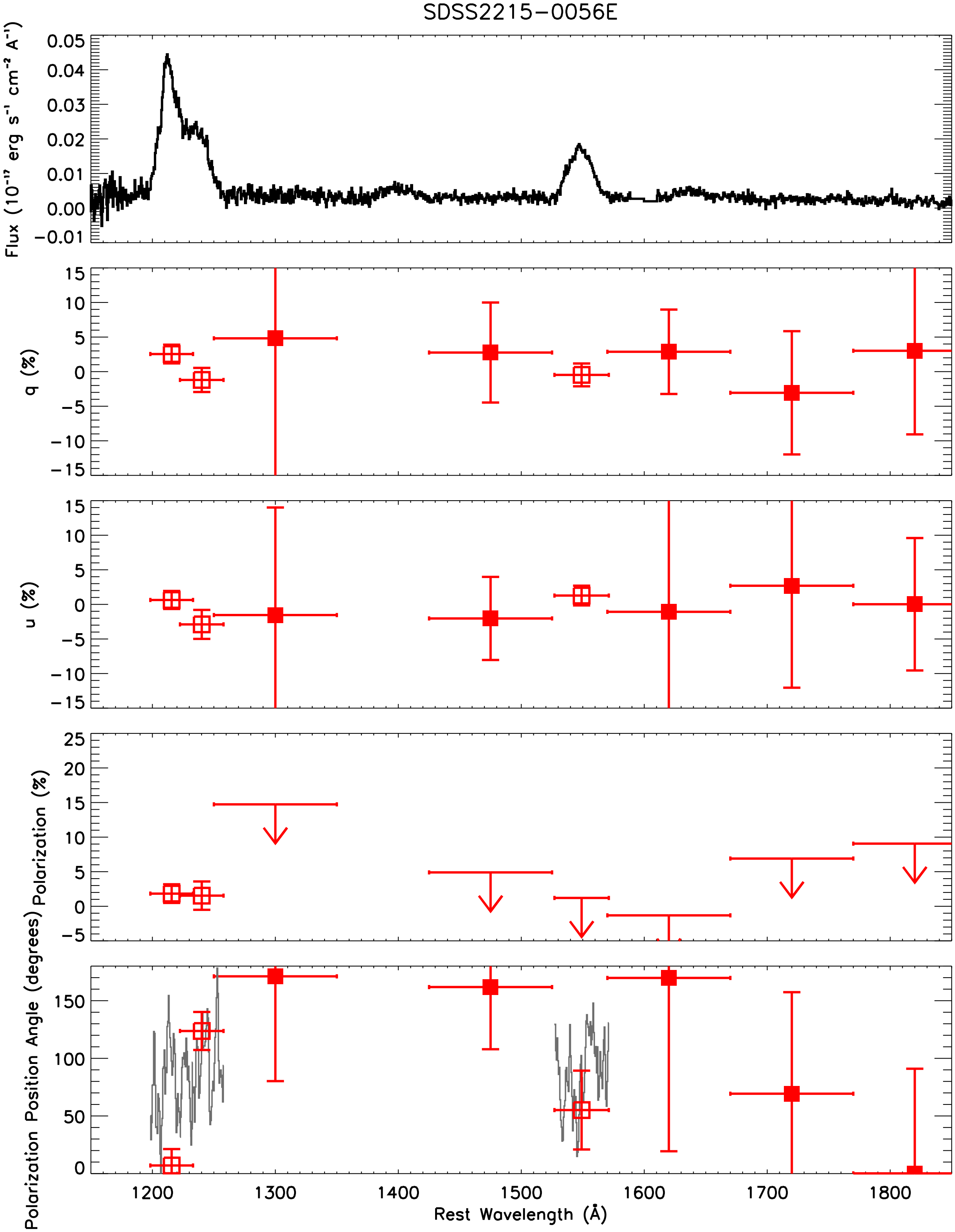

Figure A1. cont.

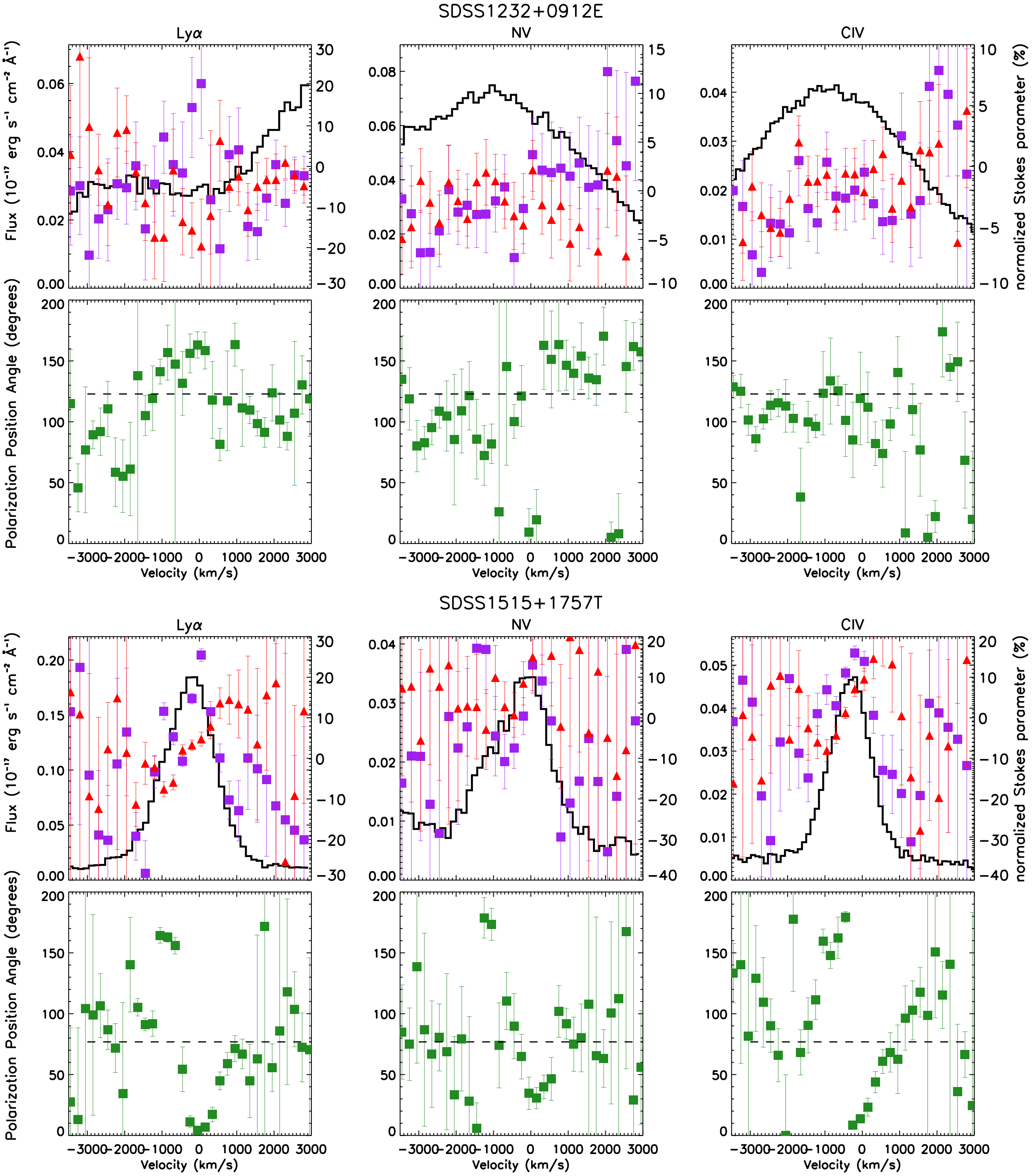

Figure A2. Emission line spectra of remaining targets (see Fig. 3).

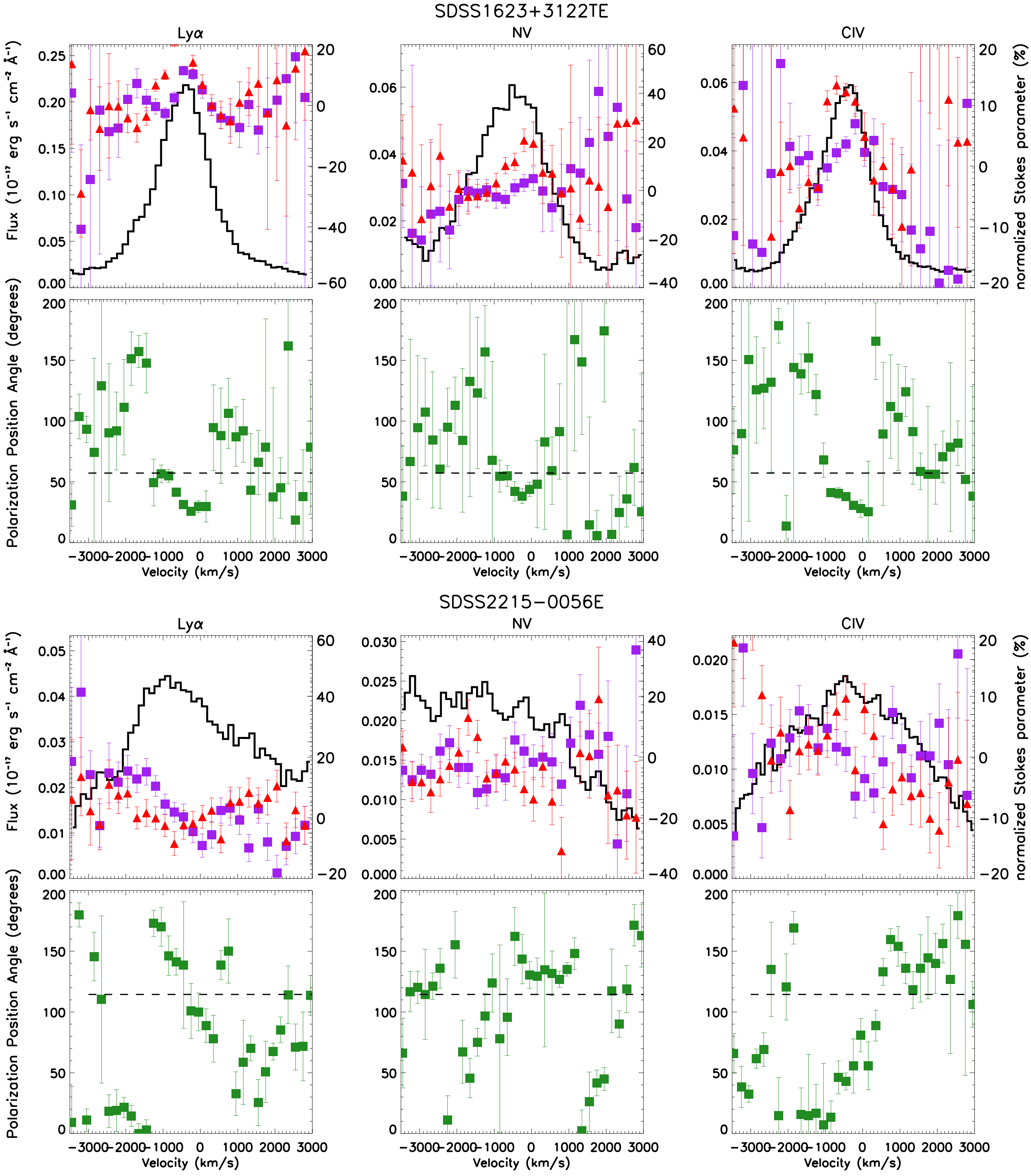

Figure A2. cont.